CCDC50 promotes tumor growth through regulation of lysosome homeostasis

Penghui Jia[1,†] , Tian Tian[2,†] , Zibo Li[1] , Yicheng Wang[1] , Yuxin Lin[1] (iD), Weijie Zeng[1] , Yu Ye[1] (iD),
Miao He[1] , Xiangrong Ni[3] , Ji'an Pan[1] , Xiaonan Dong[4] (iD) , Jian Huang[5] , Chun-mei Li[1,*] (iD),
Deyin Guo[4,**] (iD) & Panpan Hou[1,6,***] (iD)

Abstract

The maintenance of lysosome homeostasis is crucial for cell growth. Lysosome-dependent degradation and metabolism sustain tumor cell survival. Here, we demonstrate that CCDC50 serves as a lysophagy receptor, promoting tumor progression and invasion by controlling lysosomal integrity and renewal. CCDC50 monitors lysosomal damage, recognizes galectin-3 and K63-linked polyubiquitination on damaged lysosomes, and specifically targets them for autophagy-dependent degradation. CCDC50 deficiency causes the accumulation of ruptured lysosomes, impaired autophagic flux, and superfluous reactive oxygen species, consequently leading to cell death and tumor suppression. CCDC50 expression is associated with malignancy, progression to metastasis, and poor overall survival in human melanoma. Targeting CCDC50 suppresses tumor growth and lung metastasis, and enhances the effect of BRAF[V600E] inhibition. Thus, we demonstrate critical roles of CCDC50-mediated clearance of damaged lysosomes in supporting tumor growth, hereby identifying a potential therapeutic target of melanoma.

Introduction

The integrity of lysosomes is crucial for cellular homeostasis (Settembre *et al*, 2013), and the damage of lysosomes is a severe stress condition that has been implicated in various diseases including human tumors (Papadopoulos *et al*, 2020). Tumor cells are highly dynamic, changing phenotypes and global expression profiles in response to cellular context and stress (Villanueva & Herlyn, 2008; Roesch *et al*, 2010). The lysosome-associated vesicle system, including autophagosomes, was characterized as a lineage-specific feature in tumor (Alonso-Curbelo *et al*, 2014; Garcia-Fernandez *et al*, 2016). Macroautophagy (hereafter referred to as autophagy) is a lysosome-dependent degradation pathway that targets cellular constituents to a double-membrane vesicle, named autophagosomes (Mizushima & Komatsu, 2011). In the late stage of autophagy, the outer membrane of an autophagosome fuses with a lysosome to produce an autolysosome, which leads to the degradation of the sequestered damaged organelles and misfolded proteins by lysosomal enzymes (Mizushima, 2011; Lorincz & Juhasz, 2020). Such a degradation process provides nutrients to sustain cellular homeostasis, allowing survival of cancer cells under stress conditions (Levy *et al*, 2017). In turn, damaged lysosomes could also be sequestered by autophagosomes and subsequently cleared by the process termed lysophagy (Hung *et al*, 2013; Maejima *et al*, 2013; Hasegawa *et al*, 2015). Defects in lysophagy and lysosomal biogenesis are associated with lysosome dysfunction and subsequent cell deaths (Saftig & Klumperman, 2009; Zhu *et al*, 2020). Furthermore, lysosome dysfunction can aggravate autophagy deregulation and mitochondrial damage that releases reactive oxygen species (ROS) into cytosol and further amplifies cell death (Martins *et al*, 2019). While the relationship between autophagic activity and tumor is complex, autophagy has aroused an increasing interest as a target for tumor therapy (Levy *et al*, 2017). Accumulating evidence demonstrates that blocking autophagy flux not only sensitizes tumors to chemotherapy (Yang *et al*, 2011) but also improves the immunosuppressive tumor microenvironment (Noman *et al*, 2011, 2012; Baginska *et al*, 2013; Mgrditchian *et al*, 2017). More importantly, targeting autophagy further potentiates the efficacy of antitumor therapies in the treatment of melanoma (Li *et al*, 2015; Bao *et al*, 2020; Du *et al*, 2020).

1   MOE Key Laboratory of Tropical Disease Control, Centre for Infection and Immunity Study (CIIS), School of Medicine, Sun Yat-sen University, Shenzhen, China
2   The Center for Applied Genomics, Abramson Research Center, The Children's Hospital of Philadelphia, Philadelphia, PA, USA
3   Department of Neurosurgery/Neuro-oncology, Sun Yat-sen University Cancer Center, State Key Laboratory of Oncology in South China, Guangzhou, China
4   Guangzhou Laboratory, Guangzhou International Bio-Island, Guangzhou, China
5   Coriell Institute for Medical Research, Camden, NJ, USA
6   State Key Laboratory of Respiratory Disease, National Clinical Research Center for Respiratory Disease, Guangzhou Institute of Respiratory Health, The First Affiliated Hospital of Guangzhou Medical University, Guangzhou, China
   *Corresponding author. Tel: +86 020 87335462; E-mail: lichm8@mail.sysu.edu.cn
   **Corresponding author. Tel: +86 020 87335462; E-mail: guo_deyin@gzlab.ac.cn
   ***Corresponding author. Tel: +86 020 87335462; E-mail: houpp@mail.sysu.edu.cn
   †These authors contributed equally to this work

Cutaneous melanoma is a highly aggressive and refractory human cancer that is recognized as the deadliest form of skin cancer (Pavri *et al*, 2016; Apalla *et al*, 2017). In recent years, much has been explored on the genetic basis of melanoma tumorigenesis, progression, metastasis, and responses to therapy (Rabbie *et al*, 2019). Melanoma contains the highest mutational rate in cancer, and therefore, inhibitions on some gain-of-function genes including BRAF, RAS, and NF1 have been used to develop melanoma treatment (Hodis *et al*, 2012; Cancer Genome Atlas, 2015; Gutierrez-Castaneda *et al*, 2019; Yin *et al*, 2019). Among them, the mutation of V600E in BRAF (BRAF^{V600E}) is present in about 35–50% of melanoma, making it the most attractive therapeutic target. Vemurafenib (PLX4032) which was developed against BRAF^{V600E} led to a huge breakthrough in clinical treatment of melanoma (Sosman *et al*, 2012; Kim & Cohen, 2016). However, tumor resistance to vemurafenib occurs within several months of initial treatment (Czarnecka *et al*, 2020). Thus, there is an urgent need to identify alternative targets.

The coiled-coil domain-containing (CCDC) proteins have been implicated in a variety of physiological and pathological processes (Priyanka & Yenugu, 2021), such as endosomal trafficking (Wang *et al*, 2021), DNA damage repair (Kim *et al*, 2007), and tumor malignancy (Park *et al*, 2012; Tanouchi *et al*, 2016; Yang *et al*, 2020; Lu *et al*, 2021). Our previous study demonstrates that CCDC50 is a novel autophagy cargo receptor that delivers K63 polyubiquitination-activated substrates for autophagic degradation (Hou *et al*, 2021b). CCDC50 is a multifunctional regulator involved in growth factor signaling, inflammation, cell death, and cell proliferation (Tsukiyama *et al*, 2012; Hou *et al*, 2021a). Furthermore, a number of studies suggest that CCDC50 is crucial for cell survival for several cancers, including mantle cell lymphoma, chronic lymphocytic leukemia (Farfsing *et al*, 2009), and hepatocellular carcinoma (Wang *et al*, 2019). However, the precise function of CCDC50 in a specific tumor microenvironment as well as the delicate mechanism through which CCDC50 facilitates tumor growth and invasion remains elusive.

In this study, we demonstrate that CCDC50 functions as a lysophagy receptor that specifically recognizes the damaged lysosomes in tumor cells and delivers them for autophagic degradation, which is crucial for tumor progression. Deficiency of CCDC50 leads to the accumulation of damaged lysosomes and reduction in autophagic flux, consequently triggering dramatic cell apoptosis due to cellular ROS accumulation. Thus, this study reveals a previously unknown lysophagy-mediated mechanism in supporting tumor growth and indicates that CCDC50-mediated lysophagy may represent a promising target for developing effective therapies for melanoma and, potentially, other tumors.

Results

CCDC50 is highly expressed in human melanoma and associated with tumor progression

CCDC50 was identified as an autophagic cargo receptor in our previous study (Hou *et al*, 2021a,b). Given the importance of autophagy activity in tumorigenesis and progression, we evaluated the expression of CCDC50 in pan-cancer samples through analysis of the

Cancer Genome Atlas (TCGA) database and Genotype-Tissue Expression database (GTEx) (Fig EV1A). As shown in Fig 1A, the expression level of CCDC50 mRNA was significantly higher in human skin cutaneous melanoma (SKCM) than non-tumor normal tissues. Strikingly, CCDC50 expression was further elevated in metastatic samples in comparison with primary tumor specimens (Fig EV1B), and its level increased with the progression of tumor metastasis in the TCGA dataset (Fig 1B).

To further validate the protein level of CCDC50, tissue microarray (TMA) analysis of melanoma clinical specimens was performed, and it showed that the protein level of CCDC50 in primary tumor specimens was higher compared with benign dermal nevi, with a further increase in metastatic tumors (Fig 1C and D). Next, we performed histopathological analyses to assess the physiological relevance of CCDC50 expression in melanoma. Higher CCDC50-expressing melanoma lesions showed higher Ki67 staining, which is indicative of a higher cell proliferative rate (Fig 1E and F). Notably, in primary melanoma patients in the TCGA dataset, Kaplan–Meier survival analysis showed that patients with high CCDC50 expression displayed unfavorable overall survival (Fig 1G). Taken together, these findings indicate that CCDC50 is highly enriched in malignant cells in melanoma, with a further increase in expression in metastases, which may contribute to melanoma progression and invasion and is associated with unfavorable overall survival.

We then assessed genomic status of CCDC50 using TCGA data. No significant mutations were found in the CCDC50 locus (Fig EV1C). To explain why CCDC50 is highly expressed in melanoma cells, we evaluated the epigenetic and transcriptional changes in CCDC50. The analysis showed that the DNA methylation level of CCDC50 was negatively correlated with CCDC50 expression using different methylation probes (Fig EV1D). Interestingly, CCDC50 also showed a lower DNA methylation level in metastases than that in primary samples (Fig EV1E). These findings suggest that the elevated expression of CCDC50 in melanoma is not due to gene mutations but probably epigenetic changes.

CCDC50 deficiency abrogates the growth of tumor cells

To investigate the significance of CCDC50 in melanoma cell survival, we introduced short hairpin interfering RNA (shRNA) into human melanoma cell line A375 and mouse melanoma cell line B16-F10. The ablation of CCDC50 was confirmed by Western blot and real-time quantitative PCR (qRT–PCR) (Figs 2A and EV1F and G). The CCDC50-deficient cells represented the state of apoptosis and showed a significant reduction in cell growth (Fig 2B and C). We also evaluated the long-term influence of CCDC50 ablation by colony formation assay and observed that CCDC50-deficient melanoma cells exhibited decreased colony-forming capability compared with control cells (Fig 2D and E). Then, we examined the impact of CCDC50 on tumor migration and invasion. Matrigel invasion assays showed that knockdown of CCDC50 reduced the capacity of migration and invasion of melanoma cells (Fig 2F–I). Moreover, CCDC50-depleted cells also displayed decreased migration ability in scratch assays (Fig EV1H and I). On the contrary, the melanoma cells that stably overexpress CCDC50 showed statistically significant increased capability of growth and migration compared to the wild-type
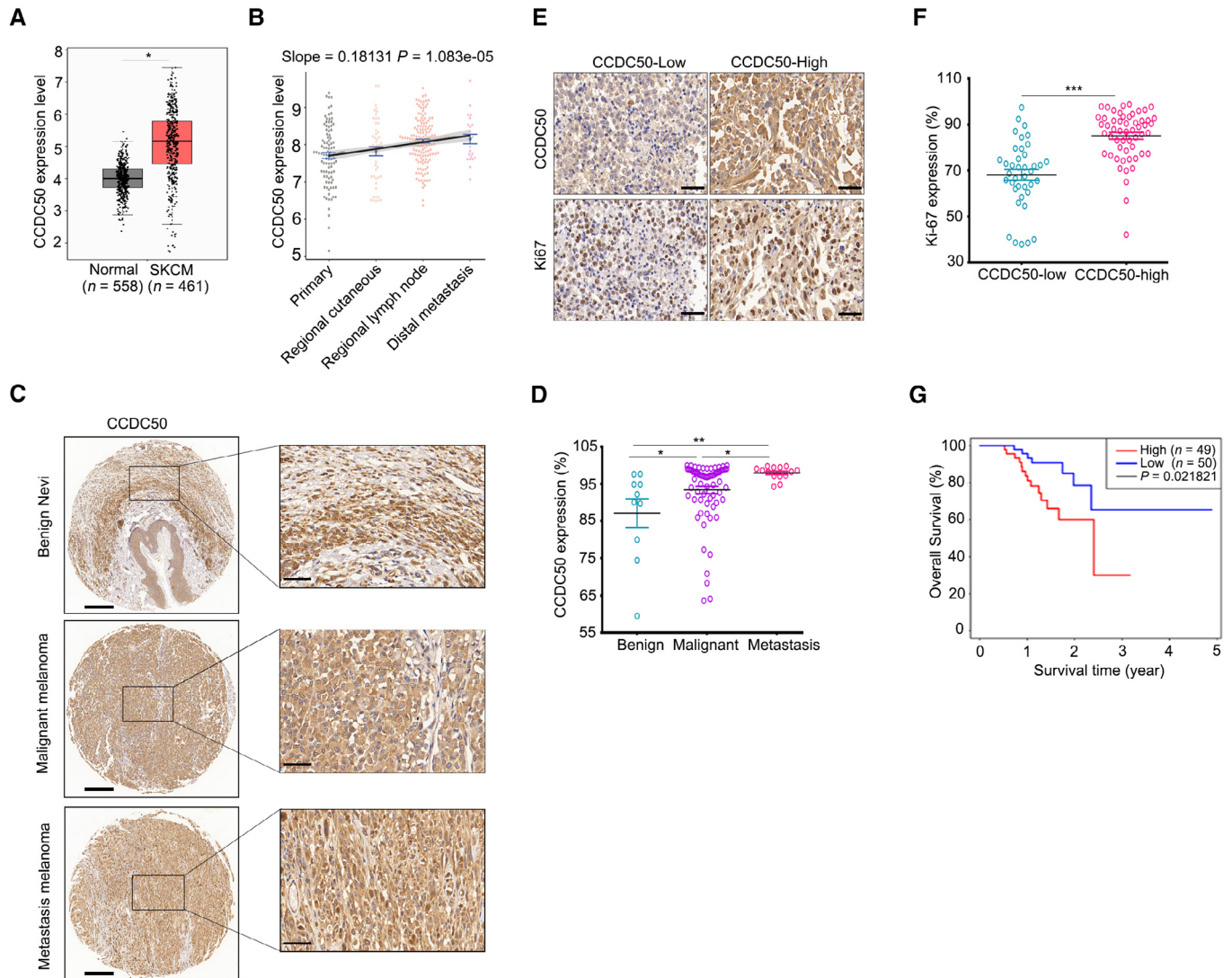
Figure 1. CCDC50 expression positively correlates with melanoma progression.

A Boxplot of CCDC50 mRNA expression in skin cutaneous melanoma (SKCM) ($n = 461$) and normal samples ($n = 558$) in TCGA and GTEx datasets. Boxplots display the distribution of data by presenting the inner fence (the whisker, taken to 1.5× the interquartile range, or IQR, from the quartile), first quartile, median, third quartile, and outliers.

B CCDC50 mRNA levels of primary and different metastases in the melanoma from TCGA dataset (primary to distal metastases: $n = 99, 50, 129$, and 43). The correlation between CCDC50 and metastasis stages is quantified by linear regression. The slope and P-value of linear regression are also plotted.

C Representative images of CCDC50 immunohistochemistry in TMA including human dermal nevi, and malignant melanocytic tumors. Scale bars, 200 μm; insert scale bar, 50 μm.

D Quantity analysis of percentage of CCDC50-positive cells in benign dermal nevi ($n = 10$), malignant ($n = 76$) and metastasis tumors ($n = 14$) in TMA samples.

E Representative images of Ki67 expression in melanoma sections classified as low and high CCDC50 expression based on below and above the 50th percentile. Scale bars, 50 μm.

F Quantity analysis of percentage of Ki67-positive cells in histological sections of human melanocytic lesions classified as in (E) (CCDC50-high, $n = 55$; CCDC50-low, $n = 39$).

G Kaplan–Meier analysis of overall survival of primary TCGA patients ($n = 99$) based on CCDC50 mRNA levels, which were stratified into two cohorts: below and above the 50th percentile (here labeled as low and high CCDC50 mRNA).

Data information: Data are shown as mean with SEM (B, D and F). Two-tailed unpaired Student's t-test. *$P < 0.05$, **$P < 0.01$, ***$P < 0.001$; log rank Mantel–Cox test was used for overall survival curve (G). See also Fig EV1.

Source data are available online for this figure.

control cells (Fig EV1J and K), suggesting that CCDC50 specifically promotes tumor cell growth and invasion. Taken together, these data demonstrate the dependency of melanoma cell growth on CCDC50.

CCDC50 favors tumor growth and metastasis *in vivo*

We next evaluated the pro-tumorigenicity activity of CCDC50 using xenograft mouse models, including subcutaneous transplantation of
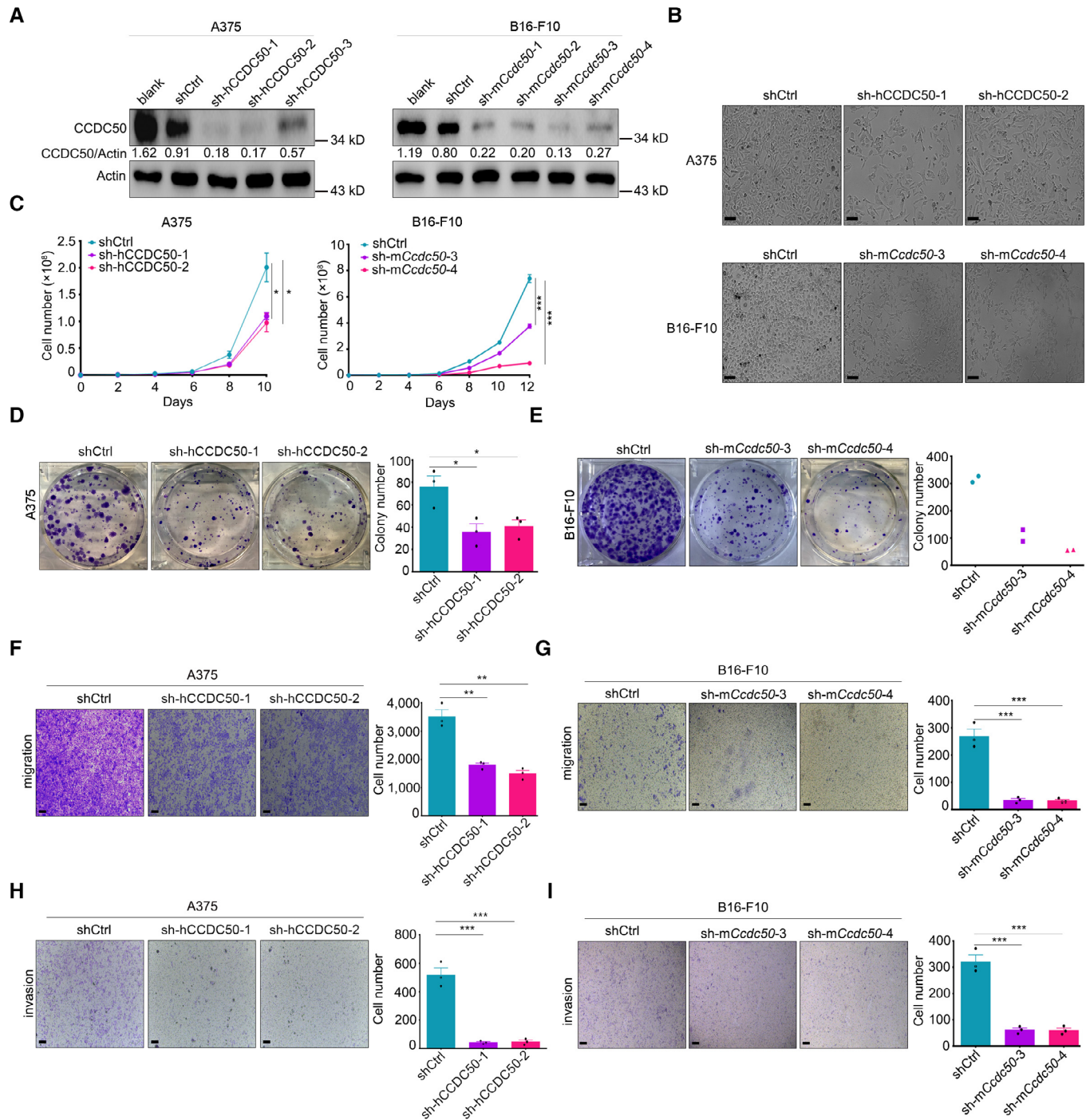
Figure 2.

A375 cells into immune-deficient nude mice and subcutaneous transplantation of B16-F10 cells into immune-competent and syngeneic C57BL/6J mice. Notably, A375 tumor-bearing nude mice expressing shCCDC50 exhibited retarded tumor growth, as indicated by decreased tumor volume and tumor weight, compared with control mice expressing shCtrl (Fig 3A–C). Similarly, we constructed shCtrl and sh*mCcdc50* B16-F10 mouse tumor cells and transplanted these cells into recipient C57BL/6J mice. The xenografts formed by

Ccdc50-depleted cells exhibited slower growth than control tumors (Fig 3A–C). Furthermore, CCDC50 deficiency inhibited melanoma development as defined by lower staining for Ki67, the proliferation index (Fig 3D). An intravenous injection model was then established to examine the effect of CCDC50 on tumor metastasis *in vivo*. A375 cells with bicistronic plasmid simultaneously expressing luciferase and shCCDC50 or shCtrl were injected intravenously into nude mice. A significant alleviation in metastasis was observed in

Figure 2. CCDC50 ablation inhibits growth and invasion of tumor cells.

A   Immunoblot analysis of CCDC50 expression in wild-type, non-targeting scramble shRNA control (shCtrl) and CCDC50 targeting human A375 cells (sh-hCCDC50) and mouse B16-F10 cells (sh-m*Ccdc50*).
B   Bright-field images of A375 cells expressing sh-hCCDC50 or B16-F10 expressing sh-mCcdc50 and their corresponding controls; scale bars, 50 µm.
C   Cell viability assays of A375 and B16-F10 cells generated as in (A). The equal number of cells carrying different shRNAs were plated on day 0 and the cell number was determined every 2 days (*n* = 3 biological replicates).
D, E   Colony formation assays of CCDC50-knockdown cells and their control cells and the colony numbers were represented on the right panels (*n* = 2 biological replicates).
F, G   Trans-well assay detection of the migration in A375 (F) and B16-F10 (G) cells with CCDC50 knockdown. The respective quantitative analysis was represented on the right panel. Representative images are shown and scale bars represent 200 µm (*n* = 3 biological replicates).
H, I   Matrigel assay detection of the invasion abilities in A375 (H) and B16-F10 (I) cells with CCDC50 knockdown. The respective quantitative analysis was represented on the right panel. Representative images are shown and scale bars represent 200 µm (*n* = 3 biological replicates).

Data information: Data are representative of three individual experiments and shown as mean with SEM (C–I). Two-tailed unpaired Student's *t*-test. *P* < 0.05,
**P* < 0.01, ***P* < 0.001. See also Fig EV1.
Source data are available online for this figure.

CCDC50-deleted group as detected by bioluminescent (BLI) image systems at day 26 after transplantation (Fig 3E).

Subsequently, in the lung colonization model, the C57BL/6J mice were transplanted with sh-m*Ccdc50* cells and shCtrl cells intravenously. The ablation of CCDC50 resulted in reduced numbers of tumor nests in the lungs of mice bearing sh-m*Ccdc50* cells compared to those of mice bearing shCtrl cells, suggesting that CCDC50 positively regulated the lung colonization of B16-F10 melanoma cells (Fig 3F and G). In addition, hematoxylin–eosin (HE) staining confirmed that tumor nests invaded the lungs, and the metastatic lesions in CCDC50-depleted groups were much fewer and smaller (Fig 3H). More importantly, mice bearing CCDC50-knockdown tumor cells exhibited improved survival time (Fig 3I).

To further validate the above results, A375 cells stably expressing inducible shRNAs against CCDC50 or non-target scrambled sequence were developed. Immunoblot analysis confirmed the reduced expression of the CCDC50 after doxycycline (DOX) treatment (Fig 3J). We transplanted the same amount of A375-Tet on shCtrl and shCCDC50 cells into the nude mice and treated the mice with DOX after the tumor developed to the threshold of 100 mm³ (Fig 3K). In contrast to direct knockdown cells (Fig 3A), the inducible cells showed no difference in tumor growth on day 15 without DOX treatment (Fig 3L). However, DOX-induced CCDC50 ablation also significantly inhibited the tumor growth, as evidenced by the growth curves of the xenograft tumors, tumor volumes, and tumor weights (Fig 3L–N). Collectively, these findings show that the deficiency of CCDC50 resulted in reduced melanoma growth and metastasis and better animal survival, thus supporting the pro-tumorigenic activities of CCDC50.

Analysis of global gene expression profiles reveals that CCDC50 sustains tumor cell survival

To investigate the potential mechanism of CCDC50 in regulating melanoma progression, we determined the global gene expression profiles with or without CCDC50 knockdown in A375 cells. We performed the differential expression analysis and gene set enrichment analysis (GSEA) with the RNA-sequencing (RNA-seq) data. At false discovery rate (FDR) level of 0.1 and nominal *P*-value < 0.005, we identified 363 Gene Ontology (GO) terms enriched in differentially regulated genes upon CCDC50 knockdown (Fig EV2A).

Figure 3. CCDC50 promotes tumor progression and metastasis *in vivo*.

A   A375 cells (left panel) and B16-F10 cells (right panel) stably expressing shCCDC50 or their respective control (shCtrl) were subcutaneously inoculated into nude mice (*n* = 12 each group) or C57BL/6J mice (*n* = 7 each group), respectively. The growth curves of tumors are shown.
B   Representative images of tumors isolated from nude (top panel) and C57BL/6J mice (bottom panel) on euthanized day.
C   Quantification analysis of tumor weights after subcutaneous implantation in mice of the indicated melanoma cell lines expressing CCDC50 shRNA or their corresponding controls. (*n* = 12 for nude mice; *n* = 7 for C57BL/6J mice)
D   Immunohistochemistry analysis of Ki67 in xenograft tumors isolated from nude (top panel) and C57BL/6J (bottom panel) mice. Nuclei were stained in blue. Scale bars, 20 µm.
E   Bioluminescent imaging (BLI) images and quantification analysis of radiance of the visceral metastasis 26 days after intravenous injection of A375-expressing luciferase-labeled shCtrl or shCCDC50 in nude mice (*n* = 5 each group).
F   Images of lung colonization in C57BL/6J mice with intravenous injection of B16-F10 cells stably expressing shCtrl or sh-mCcdc50 (*n* = 8 each group).
G   Number of metastasized nodes in lungs isolated from C57BL/6J mice treated as in (F) (*n* = 8 each group).
H   Representative HE staining of lung sections after intravenous implantation with the A375 cells (left panel) and B16-F10 cells (right panel) expressing shCtrl or shCCDC50. Scale bars, 1,000 µm; inserts, 100 µm; black arrows, metastasis nests.
I   Kaplan–Meier survival curve of C57BL/6J mice after intravenous injection of B16-F10 cells stably expressing shCtrl or sh-m*Ccdc50* (*n* = 12 mice each group).
J   A375 cells stably expressing Tet-on-induced shRNAs against control or CCDC50 were treated with DOX at indicated doses for 2 days. The cells were collected and subjected to immunoblot analysis of CCDC50 expression.
K–N   A375 cells carrying Tet-on-inducible shRNA against control or CCDC50 were transplanted into nude mice (*n* = 9 each group). The mice were treated with DOX as indicated time points (K). The growth curves of tumor volume (L), representative images of tumors (M), and tumor weights (N) are shown.

Data information: Data are repeated at least twice and shown as mean with SEM (A, C, E, G, L, N). Two-tailed unpaired Student's *t*-test. *P* < 0.05, **P* < 0.01,
***P* < 0.001; log rank Mantel–Cox test was used for mouse survival curve (I).
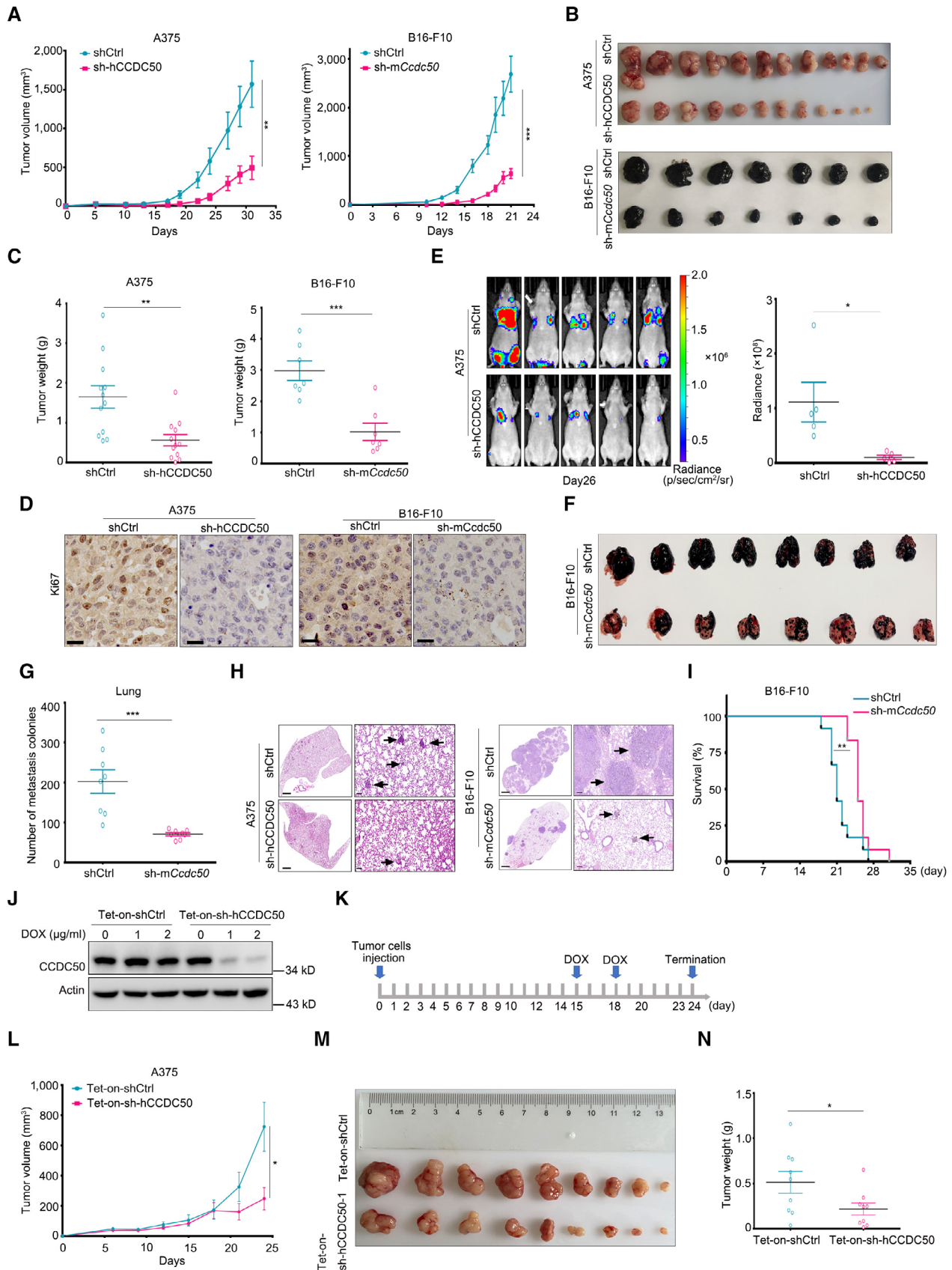Source data are available online for this figure.

Figure 3.

The upregulated pathways came from four main categories: electron complex chain, cytosolic ribosomal subunit, biosynthetic process, and lysosomes. The most significantly downregulated pathways upon CCDC50 deletion were DNA replication/repair and cell cycle (Fig 4A). In particular, DNA replication- and cell cycle-associated genes were downregulated, whereas a cluster of apoptosis- and lysosome-associated genes were enriched in shCCDC50 A375 cells (Fig EV2B).

Next, we started to validate pathways that were directly involved in cell survival, invasion, and metastasis. As shown in Fig 4B–D, depletion of CCDC50 resulted in enhanced cell apoptosis with higher propidium iodide (PI) staining, a higher percentage of annexin V-positive population, and higher caspase-3/7 activity. Further flow cytometry analysis demonstrated that CCDC50 knockdown markedly enhanced apoptosis, and the proportion of apoptosis increased over time (Fig EV2C). Consistently, A375 cells stably expressing Tet-on-inducible CCDC50 shRNA also underwent apoptosis upon CCDC50 knockdown induced by DOX treatment (Fig EV2D). In contrast, CCDC50 had no direct effect on cell cycle or cell proliferation pathways, suggesting that CCDC50 ablation affected melanoma cell growth not by regulating cell proliferation pathways but by modulating cell deaths (Fig EV2E and F). To rule out the off-target effect, we reconstituted the expression of CCDC50 in CCDC50-knockdown cells using a CCDC50-expressing plasmid that was synonymously mutated and resist to shRNA. When the expression of CCDC50 was rescued in shCCDC50 A375 cells, the apoptosis level of CCDC50-knockdown cells was restored to comparable levels of shCtrl cells (Fig EV2G). These results prove that it is the deficiency of CCDC50 that causes melanoma cell deaths.

We then used the cleavage of PARP and caspase-3 as a readout for cell apoptosis. We observed that the deficiency of CCDC50 resulted in a higher level of cleavage of caspase-3 and PARP (Fig 4E); however, the reconstitution of CCDC50 blocked the cleavage of caspase-3 and PARP in CCDC50-knockdown cells (Fig EV2H). In addition, knockdown of CCDC50 in tumor cells caused higher intratumoral apoptosis as defined by Tunnel and cleaved-caspase-3 staining (Fig 4F and G). The two well-accepted pathways of cell apoptosis include the intrinsic (or mitochondrial) and the extrinsic (or death receptor) pathways (Green & Llambi, 2015). Loss of CCDC50 caused more dramatic caspase-3 activation and PARP cleavage following treatment of BH3 mimetic ABT-737, an inhibitor of BCL2 and BCL-XL, combined with MCL-1 inhibitor cycloheximide (CHX; Fig 4H). In contrast, the cleavage of caspase-3 and PARP was not distinct in shCCDC50 and shCtrl A375 cells stimulated by TNFα plus CHX, the ligand of death receptor in extrinsic pathway, suggesting that the extrinsic death pathway may be not involved (Fig EV2I). Taken together, these results further confirm that knockdown of CCDC50 inhibits the growth of melanoma by promoting tumor cell apoptosis.

The intrinsic apoptosis pathway is accompanied by mitochondrial membrane damage, ROS production, and release of pro-apoptotic molecules such as cytochrome-c to the cytoplasm. Then, we evaluated the total cellular ROS and mitochondrial superoxide using H_2DCFDA and mitoSOX Red, respectively, in A375 cells after downregulation of CCDC50. As expected, flow cytometry and fluorescence detection showed that the total cellular ROS and mitochondrial superoxide levels were both significantly elevated after deletion of CCDC50 (Figs 4I–K and EV2J). In line with the *in vitro* results, shCCDC50 tumors showed elevated cytochrome-c release to tumor microenvironment as evidenced by immunohistochemistry (IHC) staining (Fig EV2K). Altogether, these results suggest that the deficiency of CCDC50 enhanced ROS levels and exacerbated cell apoptosis, demonstrating the pro-survival role of CCDC50 in melanoma.

Loss of CCDC50 resulted in disruption in lysosomal function and accumulation of autophagosomes

RNA-seq data further provided mechanistic insight into CCDC50 deficiency-mediated cell death. The biochemical, metabolic, and signal transduction pathways were analyzed by enrichment analysis of Kyoto Encyclopedia of Genes and Genomes (KEGG) pathways. Consistent with GSEA analysis, the results showed that 14 KEGG pathways, including oxidative phosphorylation and lysosomes, were significantly upregulated, and two pathways, including DNA replication and cell cycle, were downregulated in shCCDC50 A375 cells versus control cells (FDR < 0.1, $P < 0.005$) (Fig 5A). The results

---

Figure 4. CCDC50 ablation induces robust apoptosis in tumor cells.

A   Enrichment map for significant GO terms (nominal $P < 0.005$ and FDR < 0.1) in shCCDC50 A375 cells versus shCtrl cells ($n = 3$ each group). Nodes represent gene sets that are significantly up (red) or down (blue) regulated, as determined by GSEA, where the node size corresponds to the size of the GO term. Edges indicate overlap between gene sets, where the thickness indicates the overlap coefficient.

B   Cell death was detected with PI stain in shCCDC50 and shCtrl A375 cells. The nuclei were stained by Hoechst solution. Scale bars, 100 μm.

C   The sh-hCCDC50 and shCtrl A375 cells were incubated with FITC-Annexin V solution and subjected to FACS analysis followed by quantitative analysis of Annexin V[+] ratio ($n = 3$ biological replicates).

D   Caspase-3/7 activity analysis of sh-hCCDC50 and shCtrl A375 cells measured by caspase-GloR 3/7 assay ($n = 3$ biological replicates).

E   Immunoblot analysis of the indicated proteins in cell lysates of sh-hCCDC50 and shCtrl A375 cells. The quantification was performed by Image J software, relative to actin, and customized to nontreated shCtrl cells.

F, G   IHC analysis of Tunel (F) and cleaved-caspase-3 (G) in A375 and B16-F10 tumors stably expressing shCCDC50 or their respective control vector. Scale bars, 20 μm.

H   Immunoblot analysis of indicated proteins in sh-hCCDC50 and shCtrl A375 cells treated with BH3-mimetic ABT-737 (1 μM) plus CHX (20 μg/ml) for 3 h; the quantification was performed by Image J software, relative to actin and customized to nontreated shCtrl cells.

I   Quantification of total cellular ROS levels in sh-hCCDC50 and shCtrl A375 cells ($n = 3$ biological replicates).

J   Fluorescence images of sh-hCCDC50 and shCtrl A375 cells stained with MitoSOX red. Scale bars, 100 μm.

K   Flow cytometry analysis of mitochondrial superoxide levels in sh-hCCDC50 and shCtrl A375 cells ($n = 3$ biological replicates).

Data information: Data are representative of three individual experiments and shown as mean with SEM (C–D, I, K). FL, full length; the full and cleaved PARP and caspase-3 were developed from the same blots and were cut in case of overexpression of full-length proteins. Actin was used as a loading control. Two-tailed unpaired Student's *t*-test. *$P < 0.05$, **$P < 0.01$, ***$P < 0.001$. See also Fig EV2.
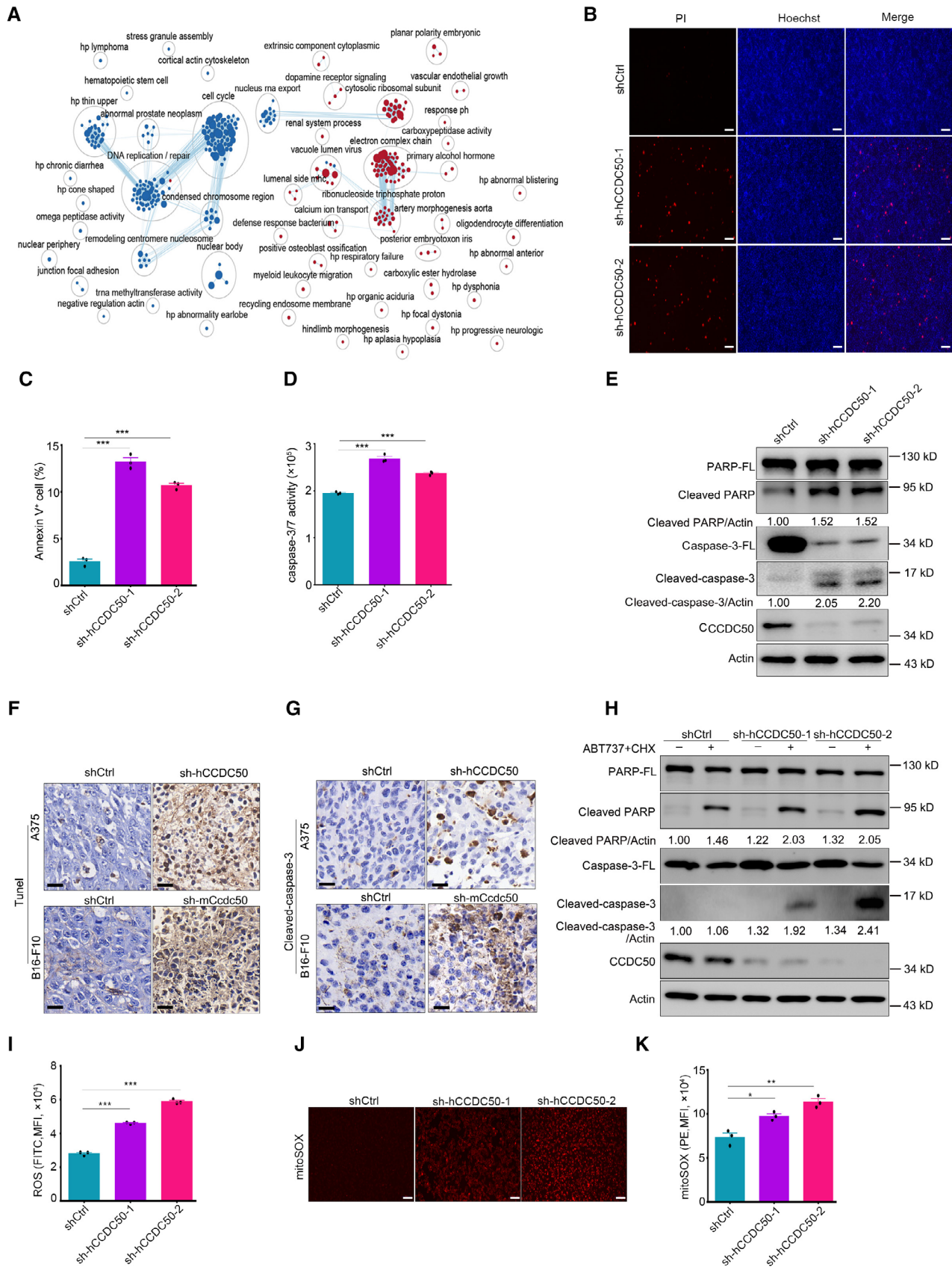Source data are available online for this figure.

Figure 4.

suggested that CCDC50 may be involved in the lysosome regulation and mitochondrial homeostasis. We then focused on autophagy–lysosome-related genes since plentiful related genes were altered upon CCDC50 knockdown in A375 cells (Figs 5B and EV3A).

Given the critical roles of CCDC50 in autophagy, we then examined the autophagy status in A375 tumor cells. Notably, LC3-II, a hallmark for autophagosomes; p62, the substrate of autophagy; and COXII, the substrate of mitophagy were all accumulated in CCDC50-deleted cells (Fig 5C). Interestingly, loss of CCDC50 also increased the expression of CTSB and CTSD, two lysosomal cathepsins. Moreover, in the presence of rapamycin, an inducer of autophagy, the discrepancy in LC3-II and p62 levels was aggravated in shCCDC50 and control cells (Fig 5D). However, the treatment of chloroquine (CQ) or bafilomycin A1 (BafA1), inhibitors of autophagy, did not further increase LC3-II and p62 levels in CCDC50-deficient cells compared with the control, although CCDC50 knockdown alone increased the levels of these two proteins (Figs 5E and EV3B). Moreover, CCDC50 depletion led to the accumulation of autophagosome-associated LC3 lipidation in both basal and induced conditions as shown by confocal microscopy (Fig EV3C). These data indicate that the effect of CCDC50 knockdown on the levels of LC3-II and p62 was because of inhibition of autophagic flux at the degradation stage.

We also detected CCDC50-regulated mitophagy flux and observed that CCDC50 ablation resulted in less degradation of COXII and more accumulation of LC3-II in A375 cells treated with antimycin A and oligomycin, inducers of mitophagy (Fig 5F). We further observed that CCDC50-deleted cells contained more unacidified yellow autophagosomes using the system of LC3 fused to both GFP and mCherry in which the GFP signal was quenched by lysosomal acidic pH, but the mCherry signal was still emitted after fusion of autophagosome and lysosome (Fig 5G). The treatment of rapamycin induced more red-only and less yellow LC3 puncta in shCtrl cells than those in shCCDC50 cells, further exacerbating the disparity in ratio of yellow puncta relative to red puncta. In contrast, CQ treatment cut down the discrepancy (Fig 5G and H). Taken together, these results reveal that the deficiency of CCDC50 impairs lysosomal activity and autophagic flux at late stage, thus resulting in enhanced cellular stress.

CCDC50 functions as a lysophagy receptor and cooperates with galectin-3 (Gal3) to drive clearance of damaged lysosomes

We demonstrated that CCDC50 is an autophagy receptor in our previous study. Under regular conditions, autophagy receptors do not affect autophagy flux, but we observed that CCDC50 depletion could block autophagic degradation and upregulate the expression of lysosome- and vesicles-associated genes (Fig 5). Thus, we hypothesized that CCDC50 might be a lysophagy receptor, regulating lysosomal equilibrium. To validate this hypothesis, we treated A375 cells with lysosomotropic reagent L-leucyl-L-leucine methyl ester (LLOMe). CCDC50 response was readily detected, and acute recruitment of CCDC50 to lysosomes was observed in LLOMe-treated A375 melanoma cells (Fig 6A). We then isolated lysosomal organelles through well-established LysoIP methodology (Abu-Remaileh *et al*, 2017; Jia *et al*, 2020b). A higher level of CCDC50 was identified in the affinity-purified lysosomal membrane after LLOMe-induced membrane damage through LysoIP, which was similar to the lysosome damage indicator, Gal3 (Fig 6B). Gal3 was reported to monitor lysosomal integrity by binding to glycans exposed to damaged lysosomes (Zhu *et al*, 2020; Jia *et al*, 2020b). Increased sodium tolerance 1 homolog (IST1), one of the ESCRT subunits, is also widely used as a marker of damaged lysosomes (Tan & Finkel, 2022). Here, we employed Gal3 to detect unrepaired lysosomes. We further detected whether CCDC50 and Gal3 interacted and how their interaction was affected by lysosomal damage. The result showed that both exogenous and endogenous CCDC50 could be coimmunoprecipitated with Gal3 after LLOMe treatment (Figs 6C and EV4A). The lysosomal membrane protein LAMP1 could also be precipitated by Gal3, suggesting that the interaction between Gal3 and CCDC50 may be not direct. Concomitantly, CCDC50 was recruited to Gal3-positive lysosomes and showed a clear colocalization with Gal3 and LAMP1 in A375 cells treated with LLOMe (Fig 6D). We also used super-resolution microscopy (N-STORM) to visualize the colocalization of CCDC50 with damaged lysosomes. The colocalization of CCDC50 and Gal3 or LAMP1 was clearly observed upon treatment with LLOMe (Fig 6E and F). Thus, these results strongly suggest that CCDC50 was recruited to damaged lysosomal organelles.

Figure 5. CCDC50 deficiency causes dysfunctions of autophagy–lysosome.

A   KEGG pathway analysis containing downregulated (blue) or upregulated (red) pathways upon CCDC50 deletion in A375 cells.

B   Dot plot of significant GO terms related to autophagy–lysosome in shCCDC50 versus shCtrl. X-axis was the normalized enrichment score (NES), colors represent FDR, and dot sizes represent sizes of GO terms.

C   Western blot analysis for LC3, COXII, CTSB, CTSD, and p62 in shCCDC50 and shCtrl A375 cells; the quantification was performed by Image J software, relative to actin and customized to nontreated shCtrl cells.

D   Immunoblot analysis of LC3 and p62 in shCCDC50 and shCtrl A375 cells treated with 3 μM rapamycin for 3 h. The quantity analysis was performed with Image J software, relative to actin, and customized to nontreated shCtrl cells.

E   Western blot analysis of LC3 and p62 in shCCDC50 and shCtrl A375 cells left untreated or treated with CQ (50 μM) for 6 h; the quantification was performed by Image J software and relative to actin.

F   The shCCDC50 and shCtrl A375 cells were treated with 5 μM oligomycin and 5 μM antimycin A for 16 h. The expression of LC3 and COXII was detected by immunoblot; the quantification was performed by Image J software, relative to actin, and customized to nontreated shCtrl cells.

G   Confocal microscopy analysis of shCCDC50 and shCtrl A375 cells transfected with mCherry-GFP-LC3B plasmid for 24 h, and then treated with DMSO or rapamycin (3 h) or CQ (6 h). Scale bars, 10 μm.

H   Quantification analysis of the ratio of yellow puncta in each group of (G) (*n* = 6 biological replicates).

Data information: Data are representative of three different experiments and shown as mean with SEM (H); actin was used as a loading control. NS, not significant. Two-tailed unpaired Student's *t*-test. *$P < 0.05$, **$P < 0.01$, ***$P < 0.001$. See also Fig EV3.
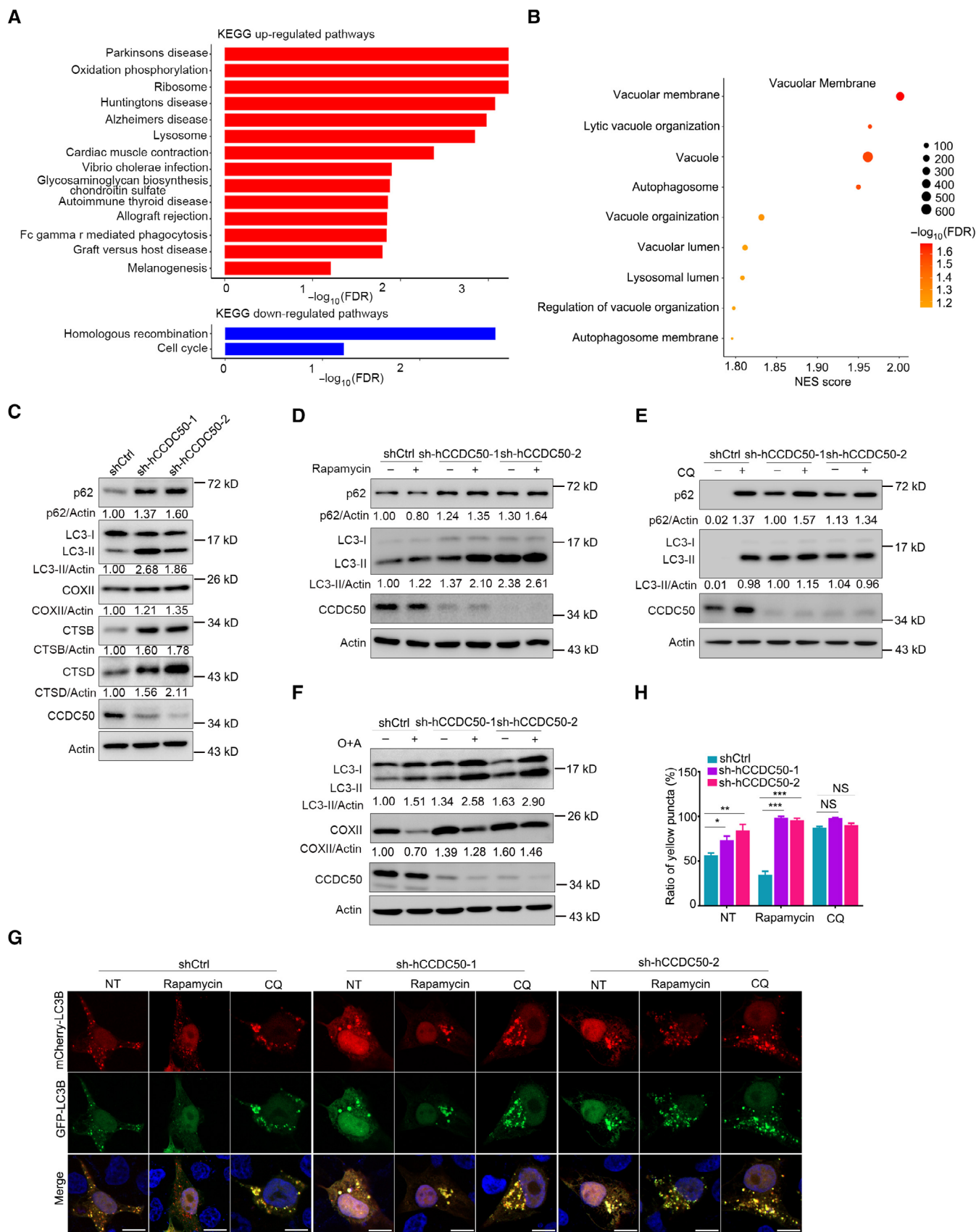
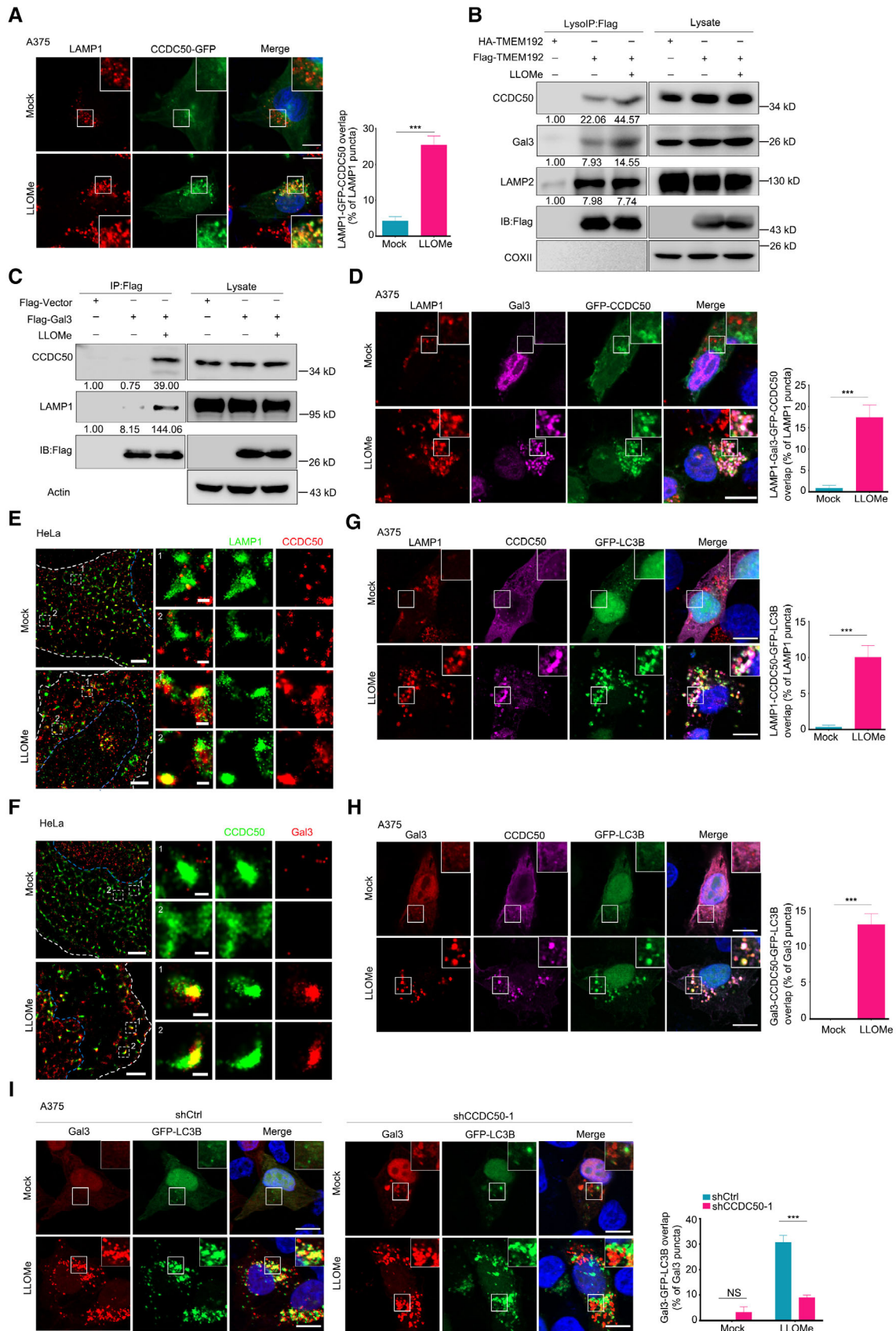Source data are available online for this figure.

Figure 5.

Figure 6.

Figure 6. Lysophagy receptor CCDC50 promotes the removal of damaged lysosomes.

A   Images and quantification analysis of the colocalization of LAMP1 and GFP-CCDC50 in A375 cells during lysosomal damage. Scale bars, 10 μm. Ten cells were counted.
B   Analysis of lysosomes isolated by anti-Flag immunoprecipitation (LysoIP: Flag-TMEM192) from HEK293T cells subjected to the 1 mM LLOMe treatment for 1 h. HA-TMEM192 was used as a negative control. The quantity analysis was performed with Image J software.
C   The endogenous interaction analysis of Gal3 and CCDC50 during lysosomal damage in HEK293T cells. The quantity analysis was performed with Image J software.
D   The overlap and quantification analysis of LAMP1, Gal3, and GFP-CCDC50 in A375 cells during lysosomal damage. Scale bars, 10 μm (*n* = 10 cells).
E, F Super-resolution microscopy analysis of CCDC50 and LAMP1 (E) and Gal3 (F) in HeLa cells untreated or treated with LLOMe for 1 h. Scale bars, 2.5 μm; inserts, 250 nm.
G   Images of the colocalization and quantification analysis of LAMP1, CCDC50, and GFP-LC3B in A375 cells during lysosomal damage. Scale bars, 10 μm (*n* = 10 cells).
H   Images of the colocalization and quantification analysis of Gal3, CCDC50, and GFP-LC3B in A375 cells during lysosomal damage. Scale bars, 10 μm (*n* = 10 cells).
I   The colocalization and quantification analysis of the interaction between Gal3 and LC3 in shCtrl and shCCDC50 A375 cells. Scale bars, 10 μm (*n* = 10 cells).

Data information: Data are representative of three different experiments and shown as mean with SEM (A, D, G–I); actin was used as a loading control. Two-tailed unpaired Student's *t*-test. ***P < 0.001. See also Fig EV4.
Source data are available online for this figure.

We then evaluated whether CCDC50 mediated the degradation of damaged lysosomes. We observed that damaged lysosomes were sensed by Gal3, further recruited CCDC50, and taken up into LC3-positive autophagosomes in A375 cells (Fig 6G and H). We developed a mutant of CCDC50, CCDC50-ΔLIR/ΔMIU that failed to bind to LC3 in our previous study (Hou *et al*, 2021b). We also detected the interaction between LC3 and Gal3 in the presence of CCDC50 or CCDC50-ΔLIR/ΔMIU. The result showed that CCDC50 exhibited a clear colocalization with Gal3 and LC3, while the mutant of CCDC50-ΔLIR/ΔMIU failed to recruit LC3 in A375 cells and thereby led to reduced colocalization of LC3 and Gal3 with the treatment of LLOMe (Fig EV4B). We noticed that there were still a few overlaps between Gal3 and LC3B in the presence of CCDC50-ΔLIR/ΔMIU, but the level was much lower than that in the presence of CCDC50 wild-type protein. It can be envisaged that the endogenous CCDC50 may also play a role. To further clarify the biological significance of CCDC50, we detected the colocalization between Gal3 and LC3 in shCtrl and shCCDC50 A375 cells. LC3 showed a clear colocalization with Gal3 in control cells, while the association between Gal3 and LC3 decreased significantly in shCCDC50 cells (Fig 6I). These data proved that the interaction between CCDC50 and LC3B is indispensable for the recruitment of LC3B to damaged lysosomes by CCDC50. The damage also triggered robust K63-linked polyubiquitination of lysosomes, the typical substrate of CCDC50 (Fig EV4C). We detected the interaction of Gal3 and the CCDC50 mutant of ΔMIU2, which was identified as failing to bind to K63-linked ubiquitin chains. The result showed that the mutant of CCDC50-ΔMIU2 could not recognize damaged lysosomes and the overlap between CCDC50-ΔMIU2 and Gal3 was decreased significantly compared to full-length CCDC50 protein (Fig EV4D). Therefore, the damage leads to extensive ubiquitination of multiple components of lysosomes, which recruits adapter proteins and then the autophagy machinery. Thus, CCDC50 functions as a lysophagy receptor, is recruited to damaged lysosomal organelles, and contributes to the clearance of ruptured lysosomes.

CCDC50 is crucial for cellular homeostasis after lysosomal damage and had significant effect on cell survival

To determine the significance of CCDC50 recruitment in protection of lysosomes, we monitored lysosomal quality using LysoTracker Red

(LTR) for functional lysosomal acidification in CCDC50-knockout (CCDC50-KO) and CCDC50 wild-type (CCDC50-WT) HeLa cells. In CCDC50-WT cells, the mean number of LTR$^+$ per cell reduced to a minimum level with the treatment of LLOMe and fully recovered 10 h after washout of LLOMe. However, in CCDC50-KO cells, there was a reduction in LTR$^+$ profiles without or with LLOMe treatment, and LTR$^+$ profiles recovered weakly 10 h after washout of LLOMe. When we reconstituted the expression of CCDC50 in CCDC50-KO cells, the restoration of CCDC50 rescued the levels of LTR$^+$ profiles in CCDC50-KO cells to comparable levels in wild-type control cells (Fig 7A). Similarly, we also examined the autophagic clearance of Gal3-labeled damaged lysosomes. Remarkably, CCDC50-KO cells showed a higher number of Gal3 puncta with or without the addition of LLOMe than CCDC50-WT cells. In CCDC50-KO cells, clearance of Gal3 vesicles was dramatically inhibited, and Gal3 puncta persisted for at least 10 h as shown by mean number. The reconstitution of CCDC50 in CCDC50-KO cells greatly diminished this phenotype (Fig 7B). Next, we further determined the effect of ectopic expression of CCDC50 on lysophagy by monitoring the number of Gal3 puncta. Overexpression of CCDC50 led to a faster clearance of damaged lysosomes (Fig EV4E). Altogether, these results demonstrate that CCDC50 is essential for the integrity and functions of lysosomes. Then, to verify whether CCDC50-mediated clearance of damaged lysosomes was dependent on canonical autophagy machinery, we detected the functions of CCDC50 in autophagy-defective melanoma cells with ATG7 knockdown. The results showed that knockdown of either ATG7 or CCDC50 led to accumulation of Gal3-positive damage lysosomes to the comparable magnitude, but double knockdown of ATG7 and CCDC50 failed to further increase such a phenotype (Fig 7C), indicating that CCDC50 functions through the canonical autophagy pathway. Moreover, CCDC50 depletion resulted in more drastic cell death induced by LLOMe in a dose-dependent manner, showing that CCDC50 was essential for restoration of cellular homeostasis after lysosomal damage (Fig 7D).

Then, we developed lentiviruses carrying HA-tagged full-length CCDC50, CCDC50-ΔMIU2, and CCDC50-ΔLIR/ΔMIU, respectively, and rescued the expression of CCDC50 or its mutants in shCCDC50 A375 cells. We examined the tumor cell growth and found that the reconstitution of full-length CCDC50 restored the growth of tumor cells to the level of shCtrl cells while the mutants of CCDC50 defective either in binding to K63 ubiquitin or LC3 failed to rescue the
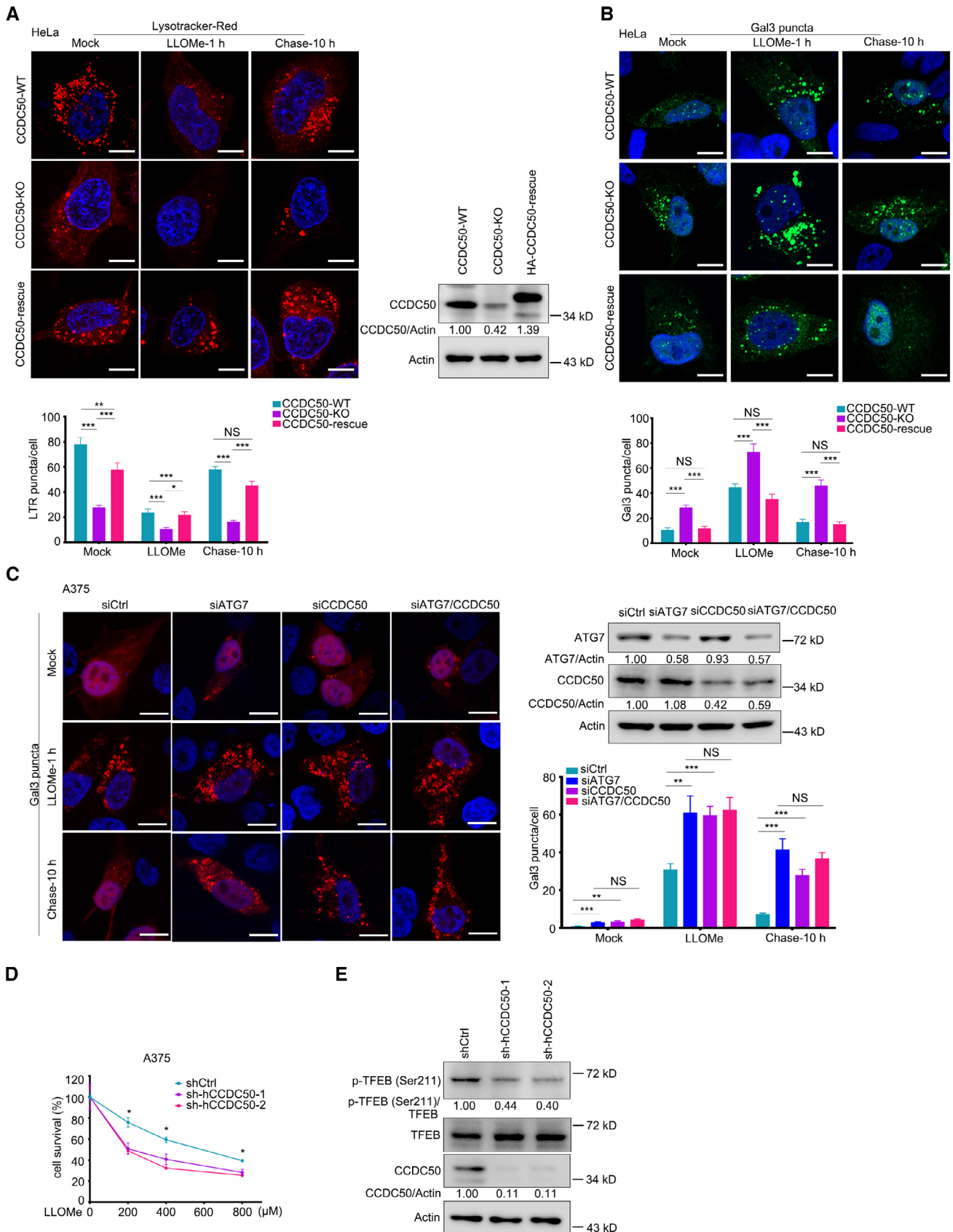
Figure 7.

Figure 7. CCDC50 is required for cell survival in response to lysosome damage.

A Status of acidified organelles in CCDC50-WT, CCDC50-KO, and CCDC50 rescued HeLa cells assessed by LysoTracker during lysosomal damage (1 mM LLOMe treatment for 1 h followed by 10 h washout). The CCDC50 expression was verified by immunoblot. LysoTracker Red (LTR) puncta in cells was quantified. Scale bars, 10 μm; 10 cells were analyzed per experiment.

B Responses of Gal3 assessed by endogenous Gal3 puncta during lysosomal damage in CCDC50-WT, CCDC50-KO, and CCDC50 rescued HeLa cells treated as in (A). Gal3 puncta was quantified and represented on the right panel. Scale bars, 10 μm; > 13 cells were analyzed per experiment.

C The status of Gal3 puncta during lysosomal damage in CCDC5-knockdown, ATG7-knockdown, and double-gene knockdown A375 cells treated with LLOMe and followed by 10 h washout. Immunoblot analysis verified the knockdown effect of ATG7 and CCDC50. And Gal3 puncta was quantified and represented. Scale bars, 10 μm; > 6 cells were analyzed per experiment.

D The shCtrl and sh-hCCDC50 cells were treated with indicated concentrations of LLOMe for 24 h. Cell viability was measured using the CCK8 assay (*n* = 5 biological replicates).

E Immunoblot analysis of p-TFEB (Ser211) and TFEB expression in shCtrl and sh-hCCDC50 A375 cells. The quantity analysis was performed with Image J software.

Data information: Data are representative of three different experiments and shown as mean with SEM (A–D); actin was used as a loading control. NS, not significant. Two-tailed unpaired Student's *t*-test. *P < 0.05, **P < 0.01, ***P < 0.001. See also Fig EV4.

Source data are available online for this figure.

tumor cell growth (Fig EV4F and G). We also collected the cells and detected the cell apoptosis. The data showed that the full-length CCDC50 expression blocked the cleavage of PARP and caspase-3 in shCCDC50 A375 cells, while the cells reconstituted with CCDC50 mutants exhibited the similar level of cell apoptosis to shCCDC50 cells (Fig EV4H). These data illustrate that CCDC50 supports the tumor cell growth dependent on the lysophagy receptor activity, and further proved the importance of CCDC50 in removing damaged lysosomes and hence cell survival.

It has been reported that lysosome damage would lead to lysosome adaptation and biogenesis by triggering nuclear translocation of transcription factor EB (TFEB) (Jia *et al*, 2020b). To substantiate the functions of CCDC50 in lysosomal homeostasis, we detected the status of TFEB in CCDC50 wild-type and knockdown melanoma cells. As expected, the phosphorylation of TFEB at site of Ser211, an indicator of inactivation of TFEB (Martina *et al*, 2012), was decreased in CCDC50 knockdown A375 cells compared to control cells, suggesting that the loss of CCDC50 triggers compensatory lysosomal biogenesis (Fig 7E). The data were consistent with our RNA-seq results that the lysosome-associated genes were enriched in CCDC50-knockdown melanoma cells. Taken together, our results demonstrate that CCDC50 functions as a lysophagy receptor and targets damaged lysosomes for autophagic degradation to promote lysosome removal and protect cells from cell death caused by the

stress caused by lysosome damage. The ablation of CCDC50 resulted in the accumulation of damaged lysosomes, leading to accumulated undegraded autophagosomes and cellular stress and, eventually, cell death.

CCDC50 ablation cooperates with BRAF^{V600E} inhibition and elicits additive effect in regression of xenografted tumors

Next, we evaluated the potential therapeutic application of targeting CCDC50 alone or together with vemurafenib (PLX4032), a clinical drug, which targets the oncogenic BRAF mutation BRAF^{V600E}. CCDC50-ablated and control cells were treated with vemurafenib, and the results showed that the ablation of CCDC50 or vemurafenib treatment alone could increase cell apoptosis and suppress tumor growth; additive growth suppression was clearly observed and had the best tumor inhibition effect, as evidenced by annexin V staining, PARP and caspase-3 cleavage, cell growth curve, and long colony formation assay (Fig 8A–D). We further detected the lysosome integrity and lysophagy activity in shCCDC50 and shCtrl melanoma cells treated with LLOMe and PLX4032. Consistent with above result, we observed that there was higher level of Gal3-labeled damaged lysosomes in CCDC50-knockdown A375 cells than those in shCtrl cells left untreated or treated with LLOMe. We then monitored the autophagic clearance of Gal3 puncta. In control cells, Gal3-positive

Figure 8. CCDC50 silencing cooperates with BRAF inhibition to elicit additive regression of xenograft tumors.

A Quantitative analysis of flow cytometry of Annexin-positive cells in shCCDC50 and shCtrl A375 cells treated with DMSO or PLX4032 (2 μM) (*n* = 3 biological replicates).

B Immunoblot analysis of indicated proteins in total cell lysates of shCCDC50 and shCtrl A375 cells treated with DMSO or PLX4032 (2 μM) for 24 h; the quantification was performed by Image J software, relative to actin and customized to nontreated shCtrl cells.

C Cell viability assay by CCK8 of shCCDC50 and shCtrl A375 cells (*n* = 3 biological replicates each group) treated with DMSO or PLX4032 (2 μM) for indicated time points.

D Colony formation assay was performed in shCtrl and shCCDC50 A375 cells (*n* = 3 biological replicates) treated with DMSO or PLX4032 (2 μM), and the number of colonies is represented in the right panel.

E–G A375 cells stably expressing shCtrl or shCCDC50 were subcutaneously injected into flanks of nude mice. When the tumor derived from shCtrl cells reached about 100 mm^3, mice were administrated with DMSO or PLX4032 at indicated time points. The growth curve of tumor (E), images of tumor (F), and tumor weights (G) are shown (*n* = 8 mice each group).

H, I The tumors in (F) were subjected to IHC to evaluate the expression of Ki67 (H) and cleaved caspase-3 (I). Scale bars, 20 μm.

J Schematic model of CCDC50-mediated lysophagy in supporting tumor growth and metastasis.

Data information: Data are repeated at least twice and shown as mean with SEM (A, C–E, G); actin was used as a loading control. Two-tailed unpaired Student's *t*-test. *P < 0.05, **P < 0.01, ***P < 0.001. See also Fig EV5.
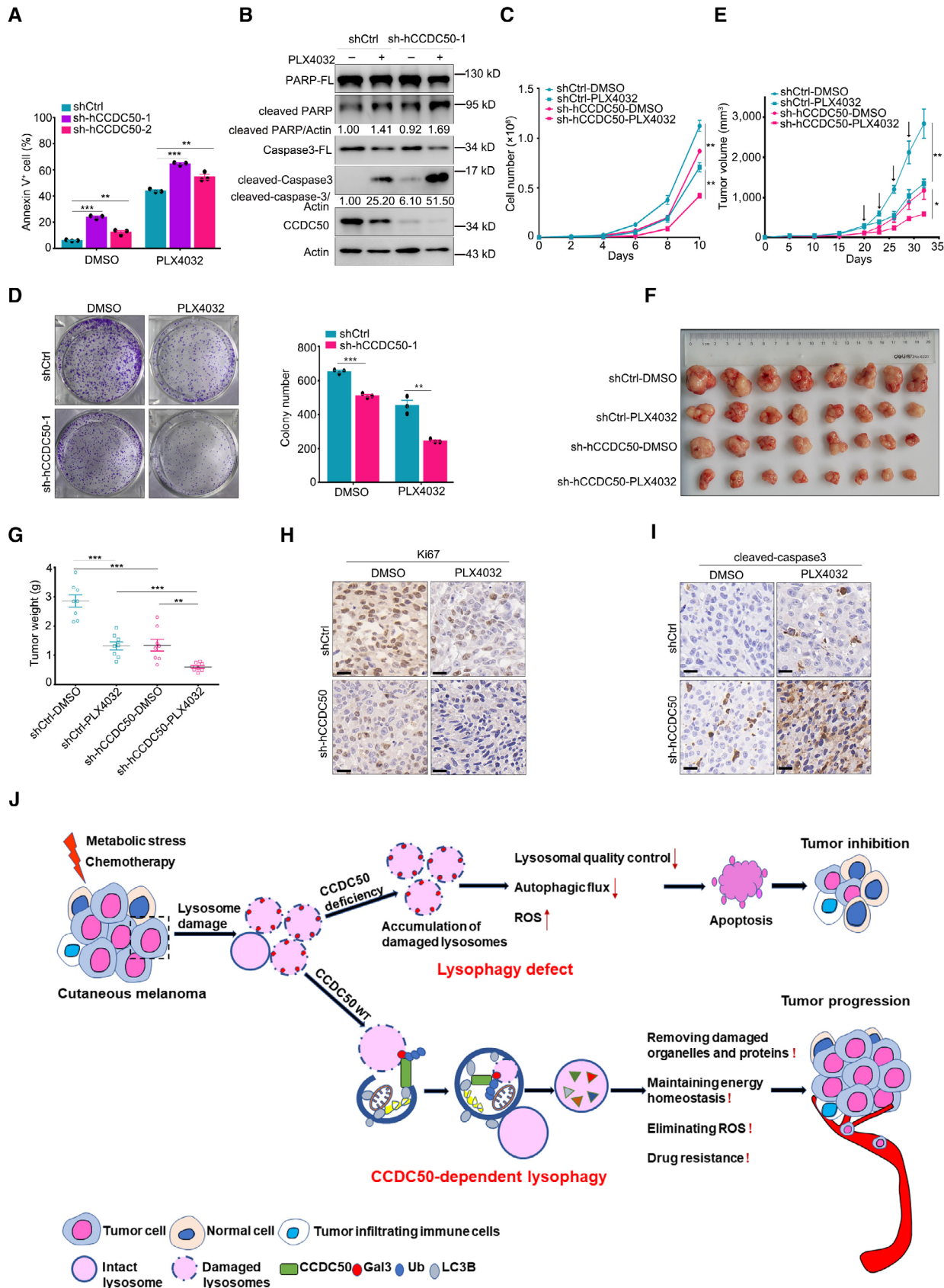
Source data are available online for this figure.

Figure 8.

lysosomes diminished 10 h after washout while in cells depleted of CCDC50, clearance of Gal3 vesicles was dramatically inhibited and Gal3 vesicles persisted for at least 10 h. More interestingly, BRAF treatment had no additive effect on shCtrl cells while led to more severe lysosome damage indicated by increased Gal3 puncta formation, suggesting that the tumor cells with lysosome damage were more sensitive to BRAF inhibition (Fig EV5A).

To determine anti-neoplastic effects of combined CCDC50 deletion with BRAF inhibition *in vivo*, the nude mice bearing tumors generated by xenografting shCCDC50 and the control A375 cells were intraperitoneally injected with vemurafenib at indicated time points. The operation on mice had no visible harm to animal health as determined by weight loss (Fig EV5B). In line with the *in vitro* results, CCDC50 silencing or vemurafenib treatment alone had obvious inhibitory effects on the growth of tumors. Nevertheless, the combination of CCDC50 targeting and vemurafenib treatment elicited more striking regression in tumor volumes, tumor sizes, and tumor weights (Fig 8E–G). Moreover, combination treatment compromised melanoma development as indicated by lower Ki67 staining for proliferation index marker and higher cleaved-caspase-3 staining for apoptosis marker (Fig 8H and I). We also pretreated shCtrl and shCCDC50 A375 cells with DMSO or vemurafenib for 48 h and transplanted these cells into the flanks of nude mice. The experiment was terminated 30 days after the transplantation. Similarly, tumors derived from vemurafenib-pretreated shCCDC50 A375 cells were smaller in size and lower in weight than those from either CCDC50-silent cells or vemurafenib-treated cells (Fig EV5C–E). IHC staining also showed lower Ki67 staining and higher cleaved caspase-3 staining in vemurafenib pretreated shCCDC50 melanoma tumors (Fig EV5F and G). Immunofluorescence assays of implanted tumors displayed that the deficiency of CCDC50 led to a dramatic increase in Gal3 puncta that colocalized with lysosomal membrane protein LAMP1, and BRAF inhibition aggravated lysosomal damage (Fig EV5H). These data show that blocking the function of CCDC50 could reduce melanoma growth and, together with BRAF^{V600E} inhibitor, achieve additive regression in melanoma growth *in vivo*.

Discussion

The tumor is a complex microecosystem involving heterogeneous cell types, genetic instability, epigenetic and transcriptomic changes, and dynamic proteomic profiles (Cancer Genome Atlas, 2015). These dynamic changes induce dramatic endogenous stress. Lysosomes are cellular metabolic factories, whose membrane rupture caused by metabolic stress can disrupt energy homeostasis. The less damaged lysosomes can be repaired by ESCRT machinery, while the severely damaged lysosomes are removed by lysophagy (Hasegawa et al, 2015; Jia et al, 2019, 2020a; Kravic et al, 2020). Here, we demonstrate that tumor cells exploit lysophagy activity to overcome oxidative stress for the benefits of their growth and migration. We also identify CCDC50 as a lysophagy receptor that recognizes and eliminates damaged lysosomes. In the absence of CCDC50, damaged lysosomes cannot be effectively removed, and lysosomal membrane rupture results in the release of lysosomal contents and eventually lysosome-dependent death. The accumulation of damaged lysosomes inhibits the functions of intact lysosomes and further blocks autophagic flux (Hasegawa et al, 2015). The defects in autophagy lead to accumulation of undigested substances and induce more oxidative stress that further induces more cell apoptosis. Thus, our study reveals a previously unknown mechanism that tumor cells exploit the CCDC50-mediated lysophagy for clearance of damaged lysosomes and sustaining their growth and survival (Fig 8J).

We found that CCDC50 is upregulated in melanoma, and the DNA methylation level of the CCDC50 gene is significantly downregulated, which further decreases in metastases and negatively correlates with CCDC50 expression, indicating that CCDC50 may act as a putative key risk factor for melanoma oncogenesis and metastasis. CCDC50 is recruited to damaged lysosomes and eliminates metabolic stress caused by aberrant proliferation of tumor cells. Previous studies that identified CCDC50 on lysosomes after lysosome damage induced by agents like LLOMe further support our findings (Koerver et al, 2019; Jia et al, 2020b). Autophagy receptors are generally thought to have no effect on autophagic flux, but loss of CCDC50 aggravates lysosome damage, resulting in severe lysosome dysfunction and impairment of lysosome-dependent degradation, including autophagy. Therefore, CCDC50 is required for maintaining lysosome homeostasis. The tumor cell is vulnerable to interruption of this degradation pathway, suggesting that CCDC50 is critical to tumor growth and invasion.

Melanoma accounts for 5% of all skin cancers but is the leading cause of skin cancer death because of its ability to metastasize at early stages of tumor development. Patients with metastatic melanoma have a 10-year survival rate of < 10% (Bhatia et al, 2015; Obeid et al, 2021). In advanced stages of melanoma, cancer cells hijack the autophagy machinery to alleviate drug-induced metabolic stress in the tumor microenvironment, thereby promoting resistance to therapies, tumor cell survival, and progression (Amaravadi et al, 2019). Therefore, targeting autophagy is a potential therapeutic approach for advanced melanoma treatment. In our research, we discover that targeting CCDC50 effectively blocks autophagic flux and lysophagy, thus providing a new target in the autophagy–lysosomal degradation pathway. We also show that targeting CCDC50 can not only accelerate ROS-induced apoptosis but also effectively inhibit visceral metastasis of melanoma and reduce the mortality caused by metastasis. The identification of lysosome/autophagy/ROS/apoptosis signaling cascades controlled by CCDC50 in melanoma has important basic and translational implications, suggesting a possibility that CCDC50 may represent a diagnostic and prognostic biomarker for melanoma.

We also employed the combination of CCDC50 ablation and BRAF^{V600E} inhibition and achieved an additive effect in accelerating apoptosis of melanoma cells in comparison with the single treatment alone. Remarkably, the combination resulted in substantial reduction in tumor burden in xenograft transplantation mouse models. These results suggest a potential role of CCDC50 in drug combination with BRAF inhibitors.

In summary, our findings reveal that lysosome-mediated degradation promotes tumor growth and metastasis, where CCDC50-mediated lysophagy plays a crucial role in timely removal of damaged lysosomes. This study emphasizes the pro-tumorigenic activity of CCDC50 in melanoma, and it may represent a promising drug target for effective melanoma therapy.

Materials and Methods

Reagents and Tools table

Reagent or resource	Source	Identifier
Antibodies		
CCDC50	Proteintech	Cat# 21082-1-AP; RRID: AB_10695770
Actin	Proteintech	Cat# 66009-1-Ig; RRID: AB_2687938
Ki67	Servicebio	Cat# GB111499
PARP	CST (Cell Signaling Technology)	Cat# 9532; RRID: AB_659884
Caspase-3	CST	Cat# 14220; RRID: AB_2798429
Cleaved Caspase-3	CST	Cat# 9661; RRID: AB_2341188
Cytochrome *c*	CST	Cat# 12963; RRID: AB_2637072
Mcl-1	CST	Cat# 94296; RRID: AB_2722740
Bcl-2	CST	Cat# 15071; RRID: AB_2744528
Bax	CST	Cat# 2772; RRID: AB_10695870
Bak	CST	Cat# 12105; RRID: AB_2716685
SQSTM/p62	CST	Cat# 39749; RRID: AB_2799160
LC3	CST	Cat# 2775; RRID: AB_915950
MTCO2	Proteintech	Cat# 55070-1-AP; RRID: AB_10859832
ATG7	CST	Cat# 2631; RRID: AB_2227783
CTSB	CST	Cat# 31718; RRID: AB_2687580
CTSD	CST	Cat# 2284; RRID: AB_10694258
Galectin-3	CST	Cat# 87985; RRID: AB_2800111
P44/42 MAPK (Erk1/2)	CST	Cat# 9102; RRID: AB_330744
Phospho-p44/42 MAPK (Erk1/2) (Thr202/Thr204)	CST	Cat# 4376; RRID: AB_331772
LAMP1	CST	Cat# 9091; RRID: AB_2687579
LAMP2	CST	Cat# 49067; RRID: AB_2799349
TFEB	CST	Cat# 4240, RRID: AB_11220225
Phospho-TFEB (Ser211)	CST	Cat#37681; RRID: AB_2799117
Flag	SIGMA	Cat# F3165; RRID: AB_259529
Flag	SIMGA	Cat# F7425; RRID: AB_439687
HA	SIGMA	Cat# H3663, RRID: AB_262051
HA	SIMGA	Cat# H6908, RRID: AB_260070
Rabbit IgG, HRP-linked antibody	CST	Cat# 7074; RRID: AB_2099233
Mouse IgG, HRP-linked antibody	CST	Cat# 7076; RRID: AB_330924
4′,6-Diamidino-2-phenylindole, dilactate (DAPI)	Thermo Fisher Scientific	Cat# D3571; RRID: AB_2307445
Goat anti-rabbit IgG (H + L) cross-adsorbed secondary antibody, Alexa Fluor 555	Thermo Fisher Scientific	Cat# A-21428; RRID: AB_2535849
Goat anti-rabbit IgG (H + L) highly cross-adsorbed secondary antibody, Alexa Fluor 647	Invitrogen	Cat# A-21245; RRID: AB_141775
Goat anti-rabbit IgG (H + L) cross-adsorbed secondary antibody, Alexa Fluor 488	Invitrogen	Cat# A-11008; RRID: AB_143165
Goat anti-mouse IgG (H + L) cross-adsorbed secondary antibody, Alexa Fluor 555	Invitrogen	Cat# A-21425, RRID: AB_2535846
Goat anti-rabbit IgG (H + L) cross-adsorbed secondary antibody, Alexa Fluor 647	Invitrogen	Cat# A-21246, RRID: AB_2535814
Goat anti-rabbit IgG (H + L) cross-adsorbed secondary antibody, Alexa Fluor 488	Invitrogen	Cat# A-11070, RRID: AB_2534114

Reagents and Tools table (continued)

Reagent or resource	Source	Identifier
Donkey Anti-mouse IgG H&L (Alexa Fluor® 405)	Abcam	Cat# ab175658; RRID: AB_2687445
Chemicals, peptides, and recombinant proteins		
Propidium iodide (PI)	SIGMA	P4170
Z-VAD	Selleck	S7023
Z-DEVD	Selleck	S7312
NAC	Selleck	S1623
TNFα	Peprotech	500-M26
Cycloheximide (CHX)	CST	2112S
Rapamycin	CST	9904S
Chloroquine	Invivogen	tlrl-chq
Bafilomycin A1	Invivogen	tlrl-baf1
Oligomycin A	Selleck	S1478
Antimycin A	Abcam	Ab141904
Lipofectamine 2000	Invivogen	11668
LLOMe	SIGMA	L7393
DMSO	SIMGA	41639
PLX4032	Selleck	S1627
Critical commercial assays		
Cell counting kit-8	Solarbio	CA1210
VivoGlo luciferin, *in vivo* grade	Promega	P1043
Cell cycle and apoptosis analysis kit	Beyotime	C1052
Annexin V-FITC apoptosis detection kit	Beyotime	C1062L
ROS assay kit	ABP Biosciences	A057
Caspase3/7	Promega	G8090
CytoPainter lysosomal staining kit-red fluorescence	Abcam	Ab112137
Mito-SOX red	Thermo Fisher Scientific	M36008
Experimental models: cell lines		
A375	ATCC	CRL1619™
B16-F10	This paper	N/A
HEK293T	This paper	N/A
HeLa	This paper	N/A
Neuro 2A	This paper	N/A
Experimental models: organisms/strains		
Mouse: C57BL/6J	Gem Pharmatech	N/A
Mouse: nude mice	Gem Pharmatech	N/A
Primers for qPCR Species	Sequence	
GAPDH Forward	Human	ATGACATCAAGAAGGTGGTG
GAPDH Reverse	Human	CATACCAGGAAATGAGCTTG
CCDC50 Forward	Human	GTCAAGGAAGTATGCCGAGATTT
CCDC50 Reverse	Human	CAAACGGTTCCGCTGAACG
Gapdh Forward	Mouse	ATGGTGAAGGTCGGTGTGAA
Gapdh Reverse	Mouse	CGCTCCTGGAAGATGGTGAT
Ccdc50 Forward	Mouse	TTCAGCGGAACCGTCTGGTA
Ccdc50 Reverse	Mouse	GCCTCAATGGTTAGCTTCTCCT

Reagents and Tools table (continued)

Reagent or resource	Source	Identifier
Recombinant DNA		
pLKO.1-puro-shRNA Control	This paper	ATGACATCAAGAAGGTGGTG
pLKO.1-puro-human-shCCDC50-1	This paper	GACCTTTGTAAACTGCCATTT
pLKO.1-puro-human-shCCDC50-2	This paper	GCGGGAGAAATCATCTTTGGA
pLKO.1-puro-human-shCCDC50-3	This paper	GAACAAGAGATTGAGCATCAT
pLKO.1-puro-mouse-shCCDC50-1	This paper	AGCTCCAGAAGCGCTACAAAG
pLKO.1-puro-mouse-shCCDC50-2	This paper	ACAAGAGATTGAGCATCATTT
pLKO.1-puro-mouse-shCCDC50-3	This paper	GCAGCTGCTTTGCTGTTTATT
pLKO.1-puro-mouse-shCCDC50-4	This paper	CACAGAAAGGCTTCCATAACA
pLKO.1-puro-luciferase-human-shCCDC50-1	This paper	GACCTTTGTAAACTGCCATTT
lentiCRISPR-v2 sgCCDC50-1	This paper	GAACGTTCAGCGGAACCGTT
lentiCRISPR-v2 sgCCDC50-2	This paper	ATTTGGCATCGAACGTTCAG
GFP-LC3	Hou et al (2021b)	N/A
mCherry-GFP-LC3	Ji'an Pan (SYSU)	N/A
GFP-CCDC50	This paper	N/A
HA-TMEM192	This paper	N/A
Flag-TMEM192	This paper	N/A
mCherry-Gal3	This paper	N/A
Flag-Gal3	This paper	N/A
HA-K63-Ub	Hou et al (2021b)	N/A
Software and algorithms		
limma R package	Bioconductor	https://bioconductor.org/packages/release/bioc/html/limma.html
GraphPad Prism version 7.0	GraphPad Software	https://www.graphpad.com/
FlowJo v10	FlowJo	https://www.flowjo.com/solutions/flowjo
Deposited Data		
Deep sequencing data	This study	GEO: GSE190144

Methods and Protocols

Cells and human tissue specimens

CCDC50-knockout HeLa cells were developed by using the CRISPR/Cas9 system with single short-guide RNA (sgRNA). The target sequences of sgRNAs were listed in Reagents and Tools table. The human melanoma cell line A375 and the other human cell lines HeLa, Neuro 2A, and 293T were cultured in Dulbecco's modified Eagle's medium (DMEM) supplemented with 10% fetal bovine serum, 1% L-glutamine (200 mM), and 1% penicillin/streptomycin. The mouse melanoma cell line B16-F10 was cultured in RPMI1640 medium supplemented with 10% fetal bovine serum, 1% L-glutamine (200 mM), and 1% penicillin/streptomycin. All cells were maintained at 37°C with 5% CO_2.

Tissue microarrays (TMA) with melanocytic tumors and control samples were purchased from Taibsbio (MME1004i)-containing dermal Nevi ($n = 10$), malignant melanoma ($n = 76$), and metastasis melanoma ($n = 14$). TMA was stained with CCDC50 and Ki67 antibodies. An automated scanning microscope and computerized image analysis system were used to calculate positive cell rate of CCDC50 and Ki67 (Aipathwell). All the human samples were used according to informed consent and ethical protocols approved by Medical Ethics Committee of Sun Yat-sen University.

Mouse models

To assess tumor growth in mouse xenograft models, 1×10^5 B16-F10 or 5×10^6 A375 cells stably expressing scrambled shRNA or shCCDC50 were subcutaneously injected (suspended in 200 μl PBS) into the back region of 4 to 6-week-old C57BL/6J or nude mice. In the inducible animal experiment, doxycycline was injected intraperitoneally at 50 mg/kg when the tumor grew to 100 mm³. At the indicated time intervals, two orthogonal external diameters were measured with a caliper. On indicated days, subcutaneous tumors were excised and weighed. Tumor volume was calculated using the formula ($a \times b^2 \times 0.5$), being "a" the longer diameter and "b" the shorter diameter of the tumor. For the metastasis models, 1.0×10^5 B16-F10 or 5×10^6 A375 cells (suspended in 100 μl PBS) were injected to 4- to 6-week-old C57BL/6J or nude mice intravenously. At indicated time points, lungs were isolated and fixed for hematoxylin–eosin staining. All animal studies were approved and supervised by the Animal Ethical and Welfare Committee of Sun Yat-sen University.

Analysis of TCGA data

Melanoma data (SKCM) in the TCGA dataset were downloaded by TCGA assembler 2 (Zhu *et al*, 2014; Wei *et al*, 2018). Since TCGA SKCM datasets contain few normal samples, comparison of CCDC50 expression levels between tumor and normal samples was conducted by combing TCGA and GTEx in the GEPIA2 tool (Tang *et al*, 2019). To compare CCDC50 expression levels between different metastasis stages, the linear regression test was conducted. Kaplan–Meier survival analysis in primary melanoma patients was conducted by dividing patients into high and low groups of CCDC50 expression levels, and the cutoff was defined as the median of expression.

Copy number variation data and DNA methylation were also downloaded by TCGA assembler 2. We defined different CNV types according to the copy number (log2 transformed) in the CCDC50 region: copy number less than −1 was defined as deep deletion, copy number greater than −1 and less than −0.5 was defined as shallow deletion, copy number > 1 was defined as amplification, copy number < 1 and > 0.5 was defined as gain, and otherwise is defined as normal diploid. The percentage of different types of CNV in all melanoma patients from TCGA datasets was summarized in the pie chart. For DNA methylation analysis in melanoma primary patients, we first correlated the delta value of probes (sites) in the CCDC50 gene region with CCDC50 expression levels by the Pearson's correlation and *P*-value. Next, we divided the primary patients into low and high groups by the expressions of CCDC50 for which the cutoff was the median. We applied *t*-test to compare the methylation levels (delta values) in the two groups and found four probes to be significant (two-tailed *t*-test *P*-value < 0.05 and absolute averaged change ≥ 0.15). We plotted the four probes by the heatmap. We also compared the DNA methylation levels (delta values) in primary and metastasis patients, and we identified four probes to be significantly changed in the two groups by the cutoff of two-tailed Wilcoxon rank-sum test *P*-value < 0.05 and absolute averaged change > 0.01.

Analysis of RNA-seq data

The quality control (trimming low bases with quality score < 20) and adaptor trimming of raw reads were conducted by trim galore (https://www.bioinformatics.babraham.ac.uk/projects/trim_galore/). Processed reads were then aligned to hg38 reference genome by HISAT2 (Kim *et al*, 2015). After obtaining BAM files, gene counts were summarized by StringTie (Pertea *et al*, 2015) with the GENCODE reference annotation. The count matrix was used as input to DESeq2 (Love *et al*, 2014) for the differential expression analysis. *P*-values of DESeq2 were corrected using the Benjamini–Hochberg procedure (Benjamini & Hochberg, 1995). The Wald statistics reported by DESeq2 were used as the input for preranked gene set enrichment analysis (GSEA) (Subramanian *et al*, 2005) of GO terms and KEGG pathways. The significant pathways were defined as FDR < 0.1 and nominal *P*-value < 0.005, and enrichment maps were built by these significant pathways in Cytoscape (Shannon *et al*, 2003). There were many similar pathways in GO terms, and similar pathways were grouped by AutoAnnotate (Kucera *et al*, 2016) with the setting that clustering algorithm was MCL clustering, edge weight was similarity coefficient, and label algorithm was WordCloud.

Plasmids and transfection

The full-length human Gal3 sequence was amplified from Neuro-2a cDNA and then cloned into pCDNA3.1-mcherry and PRK5 vectors. TMEM192 was amplified from HeLa cDNA and then cloned into PRK5 vector. CCDC50 was amplified from THP-1 cDNA and then cloned into EGFP-N1 vector. All constructs were verified by DNA sequencing. LPC-mCherry-GFP-LC3 was gifted by prof. Ji'an Pan (Sun Yat-sen University). The other plasmids used in this study were described previously (Hou *et al*, 2021b). Lentiviral packing was achieved by transfection with pSPAX2, PMD2.G, and shRNA in HEK293T cells using polyethylenimine HCl MAX (PEI, Polysciences). FuGENE® HD (Promega) and Lipofectamine 2000 (Invitrogen) were used for transient transfection of plasmids into A375 cells, HeLa cells, and Neuro-2a cells.

Gene silencing via lentiviral transduction of shRNAs

Stable knockdown of CCDC50 was achieved by lentiviral-driven gene silencing using three and four shRNAs for A375 and B16-F10 cells, respectively. The shRNAs were designed and cloned into PLKO.1 plasmid or PLKO.1-luciferase targeting the 5′-UTR or the coding sequence. Non-targeting scrambled sequence was used as a control. Lentiviruses were produced in 293T cells and transinduction was performed as previously described (Hou *et al*, 2021b). The transduced cells were selected with puromycin for another 4 days. The shRNA sequences targeting human and mouse CCDC50 are listed in Reagents and Tools table.

Quantitative RT–PCR

Total RNA was extracted with TRIzol reagent (Invitrogen). A reverse transcription system (TaKaRa) was used to synthesize cDNA. Total cDNA was subjected to real-time quantitative polymerase chain reaction using PowerUp SYBR Green PCR Master Mix (Invitrogen). Fast Real-Time PCR system (Applied Biosystems Q5) was used. GAPDH was used as a control to normalize mRNA expression. Primer sequences of qRT–PCR are listed in Reagents and Tools table.

Immunoblot analysis and immunoprecipitation

For immunoblot analysis, whole-cell extracts were collected and lysed with RIPA lysis buffer (Beyotime, P10013B). The lysates were subjected to SDS–PAGE, transferred onto PVDF membranes, and then blotted with specific antibodies. For immunoprecipitation, the cells were collected and lysed in NP-40 lysis buffer containing 20 mM Tris–HCl, pH 8.0, 150 mM NaCl, 1.0% (v/v) NP-40, 10.0% (v/v) glycerol, 2 mM EDTA, pH 8.0, and protease inhibitor cocktail (Roche). The lysate was centrifuged, and the supernatant was incubated with anti-Flag affinity gel or anti-HA affinity gel for 4 h at 4°C with precooled rotors. The affinity gel was washed three times and eluted in 2× SDS–PAGE sample buffer. The sample was boiled and loaded on SDS–PAGE. Detailed information about the antibodies used is listed in Reagents and Tools table.

LysoIP

The experimental procedure was well established previously (Abu-Remaileh *et al*, 2017). Briefly, the cells treated with or without LLOMe were quickly rinsed twice with PBS and then scraped in 1 ml KPBS (136 mM KCl and 10 mM KH2PO4, pH 7.2)

supplemented with cocktail, and centrifuged at 3000 rpm for 2 min at 4°C. The pellets were resuspended in 980 ml KPBS and reserved 80 ml for further processing of the whole-cell lysate. The remaining cells were gently homogenized with 20 strokes of a 2 ml homogenizer. The homogenate was then centrifuged at 3,000 rpm for 2 min at 4°C and the supernatant was incubated with 100 ml of KPBS prewashed anti-Flag magnetic beads on a gentle rotator shaker for 4 h. Immunoprecipitant was then gently washed three times with KPBS and eluted with 2× loading buffer and subjected to immunoblot analysis.

CCK8 assay and colony formation assay

For CCK8 assay, 1×10^5 cells were seeded into 12-well plates. 10 μl cell suspension was seeded into 96-well plates with 100 μl medium every 2 days. CCK8 solution was added (10 μl/well) and incubated for 2 h at 37°C in the dark. Absorbance was measured at 450 and 590 nm using a microplate reader. For colony formation assay, 2,000 cells in each group were seeded into 6-well plate, and 14 days later, cells were fixed with methanol and stained with 0.1% crystal violet. The number of colonies was counted.

Trans-well assay

The invasive activity of melanoma cells was determined by transwell assay using Boyden chambers (8 μm pore size; Merck Millipore, Darmstadt, Germany), according to the manufacturer's instructions. Briefly, tumor cells from each group were serum starved overnight and then seeded in 100 μl serum-free medium onto the upper chamber, and 600 μl complete fresh medium was added in the lower chamber in a 24-well plate. For migration, 1×10^5 cells were used to pass through the trans-well filter. For invasion, 2×10^5 cells were used to pass through the trans-well membranes which were pre-coated with Matrigel (BD Biosciences, 356234) prior to plating cells. The cells were cultured for 24 h followed by removal of cells inside the upper chamber with cotton swabs, and the invasive cells on the lower side were fixed and stained with crystal violet solution. Cells were scanned and the colony was counted under light microscopy.

Scratch assay

Melanoma cells stably expressing scrambled or CCDC50 shRNA were seeded into a 12-well plate. When an appropriate confluence was reached, the cell layer was scraped with a sterile pipette tip and then cultured in serum-free medium for the indicated time. Cells were imaged at different time points under a light microscope.

Hematoxylin and eosin (H&E) staining

Lungs from nude mice and C57BL/6J mice intravenously injected with melanoma cells were dissected, fixed in 4% paraformaldehyde, embedded into paraffin, sectioned, and subjected to staining with hematoxylin and eosin solution. The images were scanned with light microscopy.

Bioluminescence imaging of mouse

Bioluminescence imaging was conducted to monitor metastases using the IVIS Lumina imaging station (Caliper Life Sciences). Tumor-bearing mice were injected intraperitoneally with a luciferin solution at 150 mg/kg (potassium salt, Gold Biotechnology) before isoflurane anesthesia. The bioluminescence images were acquired

15 min after substrate injection using the IVIS Lumina system and analyzed by Living Image software.

Flow cytometry

The Annexin V-FITC Cell Apoptosis Detection Kit (Beyotime, C1062L) was used to detect apoptotic cells according to the manufacturer's protocol. In brief, cells of each group were harvested and resuspended in ice-cold PBS buffer at a concentration of 10^6 cell/ml. After the addition of 195 ul binding buffer, 5 μl FITC-labeled Annexin V and 10 μl propidium iodide (PI) were added and incubated for 20 min at room temperature. The apoptotic cells were measured by FACS analysis.

For cell cycle analysis, cells were fixed in 70% ice-cold ethanol at 4°C overnight and washed with PBS for three times. Then, the cells were resuspended in 500 μl of PBS containing propidium iodide (PI) in the dark for 30 min at room temperature according to the manufacturer's instructions (Beyotime, C1052). Cell cycle distribution was analyzed using Beckman Culter Flow Cytoflex.

For intracellular ROS analysis, cells were collected via centrifugation, resuspended in 10 μM H_2DCFDA, and incubated for 30 min at 37°C. Then, cells were washed three times with prewarmed HBSS buffer, resuspended with pre-warmed growth medium, and incubated for 10 min at 37°C. Measurement was performed immediately with a flow cytometer with 488 nm excitation.

MitoSOX Red (Thermo Fisher Scientific, M36008) was used to analyze mitochondrial superoxide production. A375 cells were seeded in a 12-well plate. One ml of 5 μM MitoSOX reagent working solution was applied to cover cells for 10 min at 37°C in the dark. The cells were washed gently three times with prewarmed HBSS buffer, followed with imaging by microscope or analyzing by flow cytometry.

PI stain

The cells were stained with propidium iodide and Hoechst (Solarbio, C0031) solution according to the manufactures' instruction. Images were scanned by fluorescence microscopy.

Enzyme activity detection of caspase-3/7

A total of 2,500 cells were seeded in a 96-well white opaque plate. Enzyme activity assay was performed using Caspase-Glo 3/7 Assay kit (Promega, G8090). The plate was subjected to luminescence detection after 2 h incubation.

Dual-color STORM imaging

HeLa cells were seeded on a glass-=bottom dish (NEST) for dual-color STORM. After transfection and drug treatment, cells were fixed, blocked, and incubated with indicated primary antibodies overnight at 4°C. The cells were then probed with goat-anti-mouse CF568 (1:1,000, 20800, Biotium) or goat-anti-rabbit AlexaFluor 647 (1:500, ThermoFisher) fluorescence-labeled secondary antibodies for 1 h at room temperature. The STORM imaging buffer was prepared as previous described (Zeng *et al*, 2020). Glucose oxidase (G2133, Sigma) and catalase (C1345, Sigma) stock solution was dissolved in Buffer A (10 mM Tris, 50 mM sodium chloride, pH 8.0) with a final concentration of 70 mg/ml and 17 mg/ml, respectively. GLOX solution was prepared freshly by mixing glucose oxidase and catalase stock solution at 4:1 ratio. The imaging buffer was freshly prepared by mixing 7 μl GLOX, 7 μl 2-mercaptoethanol (07604,

Sigma), and 690 μl Buffer B (50 mM Tris, 10 mM sodium chloride, 10% glucose, pH 8.0), and the buffer was added into the glass bottom dish before STORM imaging. Fluorescence signals of CF568 and AlexaFluor 647 were detected sequentially on a Nikon N-STORM microscope system using a 100× oil objective lens (APO TIRF, 1.49NA, Nikon) and an ORCA-Flash 4.0 V2 sCMOS camera (Hamamatsu) at 40 ms exposure in the no-binning mode. Image reconstruction was performed by Nikon NIS Element software (v5.1) with N-STORM plugin. Detailed information about the antibodies used is listed in Reagents and Tools table.

Immunofluorescence labeling and confocal microscopy

A375, HeLa, and Neuro 2A cells were seeded in glass coverslips. After transfection or stimulation, the cells were fixed with 4% paraformaldehyde, permeabilized with 0.2% Triton X-100, and blocked with 1% bovine serum albumin (BSA) in PBS. The coverslips were incubated with the indicated primary antibodies followed by fluorescent dye-conjugated secondary antibodies. Nuclei were stained with DAPI (Invitrogen). Fluorescence was visualized with a Carl Zeiss laser-scanning confocal microscope. Detailed information about the antibodies used is listed in Reagents and Tools table.

Statistical analysis

All experiments were repeated at least twice, and the data were shown as the mean with SEM. Statistical significance between different groups was calculated by two-tailed unpaired Student's t-test, Wilcoxon rank-sum test, or two-way ANOVA test. For the survival curve of mice, log-rank (Mantel–Cox) test was used for the comparison. P-value < 0.05 was considered significant. Data were analyzed with GraphPad Prism 7.0 Software.

Data availability

The raw and processed RNA-sequencing data have been deposited in the NCBI Gene Expression Omnibus (GEO) with accession number GSE190144 (https://www.ncbi.nlm.nih.gov/geo/query/acc.cgi?acc=GSE190144). They are publicly available.

Expanded View for this article is available online.

Author contributions

Panpan Hou: Conceptualization; resources; formal analysis; supervision; funding acquisition; validation; investigation; methodology; writing – original draft; project administration; writing – review and editing. **Penghui Jia:** Conceptualization; software; formal analysis; validation; investigation; methodology; writing – original draft; writing – review and editing. **Tian Tian:** Resources; data curation; software; formal analysis; methodology; writing – original draft; writing – review and editing. **Zibo Li:** Resources; validation; investigation. **Yicheng Wang:** Resources. **Yuxin Lin:** Resources. **Weijie Zeng:** Resources; visualization. **Yu Ye:** Resources; investigation. **Miao He:** Resources. **Xiangrong Ni:** Resources. **Ji'an Pan:** Resources; writing – review and editing. **Xiaonan Dong:** Methodology; writing – review and editing. **Jian Huang:** Methodology; writing – review and editing. **Chun-mei Li:** Supervision; validation; writing – review and editing. **Deyin Guo:** Conceptualization; supervision; funding acquisition; writing – original draft; project administration; writing – review and editing.

Disclosure and competing interests statement

The authors declare that they have no conflict of interest.

References

Abu-Remaileh M, Wyant GA, Kim C, Laqtom NN, Abbasi M, Chan SH, Freinkman E, Sabatini DM (2017) Lysosomal metabolomics reveals V-ATPase- and mTOR-dependent regulation of amino acid efflux from lysosomes. *Science* 358: 807–813

Alonso-Curbelo D, Riveiro-Falkenbach E, Perez-Guijarro E, Cifdaloz M, Karras P, Osterloh L, Megias D, Canon E, Calvo TG, Olmeda D *et al* (2014) RAB7 controls melanoma progression by exploiting a lineage-specific wiring of the endolysosomal pathway. *Cancer Cell* 26: 61–76

Amaravadi RK, Kimmelman AC, Debnath J (2019) Targeting autophagy in cancer: recent advances and future directions. *Cancer Discov* 9: 1167–1181

Apalla Z, Nashan D, Weller RB, Castellsague X (2017) Skin cancer: epidemiology, disease burden, pathophysiology, diagnosis, and therapeutic approaches. *Dermatol Ther (Heidelb)* 7: 5–19

Baginska J, Viry E, Berchem G, Poli A, Noman MZ, van Moer K, Medves S, Zimmer J, Oudin A, Niclou SP *et al* (2013) Granzyme B degradation by autophagy decreases tumor cell susceptibility to natural killer-mediated lysis under hypoxia. *Proc Natl Acad Sci USA* 110: 17450–17455

Bao Y, Ding Z, Zhao P, Li J, Chen P, Zheng J, Qian Z (2020) Autophagy inhibition potentiates the anti-EMT effects of alteronol through TGF-beta/Smad3 signaling in melanoma cells. *Cell Death Dis* 11: 223

Benjamini Y, Hochberg Y (1995) Controlling the false discovery rate: a practical and powerful approach to multiple testing. *J R Stat Soc Series B Methodol* 57: 289–300

Bhatia S, Tykodi SS, Lee SM, Thompson JA (2015) Systemic therapy of metastatic melanoma: on the road to cure. *Oncology (Williston Park)* 29: 126–135

Cancer Genome Atlas N (2015) Genomic classification of cutaneous melanoma. *Cell* 161: 1681–1696

Czarnecka AM, Bartnik E, Fiedorowicz M, Rutkowski P (2020) Targeted therapy in melanoma and mechanisms of resistance. *Int J Mol Sci* 21: 4576

Du J, Dong Z, Tan L, Tan M, Zhang F, Zhang K, Pan G, Li C, Shi S, Zhang Y *et al* (2020) Tubeimoside I inhibits cell proliferation and induces a partly disrupted and cytoprotective autophagy through rapidly hyperactivation of MEK1/2-ERK1/2 cascade via promoting PTP1B in melanoma. *Front Cell Dev Biol* 8: 607757

Farfsing A, Engel F, Seiffert M, Hartmann E, Ott G, Rosenwald A, Stilgenbauer S, Dohner H, Boutros M, Lichter P *et al* (2009) Gene knockdown studies revealed CCDC50 as a candidate gene in mantle cell lymphoma and chronic lymphocytic leukemia. *Leukemia* 23: 2018–2026

Garcia-Fernandez M, Karras P, Checinska A, Canon E, Calvo GT, Gomez-Lopez G, Cifdaloz M, Colmenar A, Espinosa-Hevia L, Olmeda D *et al* (2016) Metastatic risk and resistance to BRAF inhibitors in melanoma defined by selective allelic loss of ATG5. *Autophagy* 12: 1776–1790

Green DR, Llambi F (2015) Cell death signaling. *Cold Spring Harb Perspect Biol* 7: a006080

Gutierrez-Castaneda LD, Nova JA, Tovar-Parra JD (2019) Frequency of mutations in BRAF, NRAS, and KIT in different populations and histological subtypes of melanoma: a systemic review. *Melanoma Res* 30: 62–70

Hasegawa J, Maejima I, Iwamoto R, Yoshimori T (2015) Selective autophagy: lysophagy. *Methods* 75: 128–132

Hodis E, Watson IR, Kryukov GV, Arold ST, Imielinski M, Theurillat JP, Nickerson E, Auclair D, Li L, Place C *et al* (2012) A landscape of driver mutations in melanoma. *Cell* 150: 251–263

Hou P, Lin Y, Li Z, Lu R, Wang Y, Tian T, Jia P, Zhang X, Cao L, Zhou Z *et al* (2021a) Autophagy receptor CCDC50 tunes the STING-mediated interferon response in viral infections and autoimmune diseases. *Cell Mol Immunol* 18: 2358–2371

Hou P, Yang K, Jia P, Liu L, Lin Y, Li Z, Li J, Chen S, Guo S, Pan J *et al* (2021b) A novel selective autophagy receptor, CCDC50, delivers K63 polyubiquitination-activated RIG-I/MDA5 for degradation during viral infection. *Cell Res* 31: 62–79

Hung YH, Chen LM, Yang JY, Yang WY (2013) Spatiotemporally controlled induction of autophagy-mediated lysosome turnover. *Nat Commun* 4: 2111

Jia J, Abudu YP, Claude-Taupin A, Gu Y, Kumar S, Choi SW, Peters R, Mudd MH, Allers L, Salemi M *et al* (2019) Galectins control MTOR and AMPK in response to lysosomal damage to induce autophagy. *Autophagy* 15: 169–171

Jia J, Bissa B, Brecht L, Allers L, Choi SW, Gu Y, Zbinden M, Burge MR, Timmins G, Hallows K *et al* (2020a) AMPK is activated during lysosomal damage via a galectin-ubiquitin signal transduction system. *Autophagy* 16: 1550–1552

Jia J, Claude-Taupin A, Gu Y, Choi SW, Peters R, Bissa B, Mudd MH, Allers L, Pallikkuth S, Lidke KA *et al* (2020b) Galectin-3 coordinates a cellular system for lysosomal repair and removal. *Dev Cell* 52: 69–87.e8

Kim A, Cohen MS (2016) The discovery of vemurafenib for the treatment of BRAF-mutated metastatic melanoma. *Expert Opin Drug Discov* 11: 907–916

Kim H, Huang J, Chen J (2007) CCDC98 is a BRCA1-BRCT domain-binding protein involved in the DNA damage response. *Nat Struct Mol Biol* 14: 710–715

Kim D, Langmead B, Salzberg SL (2015) HISAT: a fast spliced aligner with low memory requirements. *Nat Methods* 12: 357–360

Koerver L, Papadopoulos C, Liu B, Kravic B, Rota G, Brecht L, Veenendaal T, Polajnar M, Bluemke A, Ehrmann M *et al* (2019) The ubiquitin-conjugating enzyme UBE2QL1 coordinates lysophagy in response to endolysosomal damage. *EMBO Rep* 20: e48014

Kravic B, Behrends C, Meyer H (2020) Regulation of lysosome integrity and lysophagy by the ubiquitin-conjugating enzyme UBE2QL1. *Autophagy* 16: 179–180

Kucera M, Isserlin R, Arkhangorodsky A, Bader GD (2016) AutoAnnotate: a Cytoscape app for summarizing networks with semantic annotations. *F1000Res* 5: 1717

Levy JMM, Towers CG, Thorburn A (2017) Targeting autophagy in cancer. *Nat Rev Cancer* 17: 528–542

Li J, Yang D, Wang W, Piao S, Zhou J, Saiyin W, Zheng C, Sun H, Li Y (2015) Inhibition of autophagy by 3-MA enhances IL-24-induced apoptosis in human oral squamous cell carcinoma cells. *J Exp Clin Cancer Res* 34: 97

Lorincz P, Juhasz G (2020) Autophagosome-lysosome fusion. *J Mol Biol* 432: 2462–2482

Love MI, Huber W, Anders S (2014) Moderated estimation of fold change and dispersion for RNA-seq data with DESeq2. *Genome Biol* 15: 550

Lu Y, Huang Y, Li J, Huang J, Zhang L, Feng J, Li J, Xia Q, Zhao Q, Huang L *et al* (2021) Eosinophil extracellular traps drive asthma progression through neuro-immune signals. *Nat Cell Biol* 23: 1060–1072

Maejima I, Takahashi A, Omori H, Kimura T, Takabatake Y, Saitoh T, Yamamoto A, Hamasaki M, Noda T, Isaka Y *et al* (2013) Autophagy sequesters damaged lysosomes to control lysosomal biogenesis and kidney injury. *EMBO J* 32: 2336–2347

Martina JA, Chen Y, Gucek M, Puertollano R (2012) MTORC1 functions as a transcriptional regulator of autophagy by preventing nuclear transport of TFEB. *Autophagy* 8: 903–914

Martins WK, Santos NF, Rocha CS, Bacellar IOL, Tsubone TM, Viotto AC, Matsukuma AY, Abrantes ABP, Siani P, Dias LG *et al* (2019) Parallel damage in mitochondria and lysosomes is an efficient way to photoinduce cell death. *Autophagy* 15: 259–279

Mgrditchian T, Arakelian T, Paggetti J, Noman MZ, Viry E, Moussay E, Van Moer K, Kreis S, Guerin C, Buart S *et al* (2017) Targeting autophagy inhibits melanoma growth by enhancing NK cells infiltration in a CCL5-dependent manner. *Proc Natl Acad Sci USA* 114: E9271–E9279

Mizushima N (2011) Autophagy in protein and organelle turnover. *Cold Spring Harb Symp Quant Biol* 76: 397–402

Mizushima N, Komatsu M (2011) Autophagy: renovation of cells and tissues. *Cell* 147: 728–741

Noman MZ, Janji B, Kaminska B, Van Moer K, Pierson S, Przanowski P, Buart S, Berchem G, Romero P, Mami-Chouaib F *et al* (2011) Blocking hypoxia-induced autophagy in tumors restores cytotoxic T-cell activity and promotes regression. *Cancer Res* 71: 5976–5986

Noman MZ, Janji B, Berchem G, Mami-Chouaib F, Chouaib S (2012) Hypoxia-induced autophagy: a new player in cancer immunotherapy? *Autophagy* 8: 704–706

Obeid MA, Aljabali AAA, Rezigue M, Amawi H, Alyamani H, Abdeljaber SN, Ferro VA (2021) Use of nanoparticles in delivery of nucleic acids for melanoma treatment. *Methods Mol Biol* 2265: 591–620

Papadopoulos C, Kravic B, Meyer H (2020) Repair or lysophagy: dealing with damaged lysosomes. *J Mol Biol* 432: 231–239

Park SJ, Jang HR, Kim M, Kim JH, Kwon OH, Park JL, Noh SM, Song KS, Kim SY, Kim YH *et al* (2012) Epigenetic alteration of CCDC67 and its tumor suppressor function in gastric cancer. *Carcinogenesis* 33: 1494–1501

Pavri SN, Clune J, Ariyan S, Narayan D (2016) Malignant melanoma: beyond the basics. *Plast Reconstr Surg* 138: 330e–340e

Pertea M, Pertea GM, Antonescu CM, Chang TC, Mendell JT, Salzberg SL (2015) StringTie enables improved reconstruction of a transcriptome from RNA-seq reads. *Nat Biotechnol* 33: 290–295

Priyanka PP, Yenugu S (2021) Coiled-coil domain-containing (CCDC) proteins: functional roles in general and male reproductive physiology. *Reprod Sci* 28: 2725–2734

Rabbie R, Ferguson P, Molina-Aguilar C, Adams DJ, Robles-Espinoza CD (2019) Melanoma subtypes: genomic profiles, prognostic molecular markers and therapeutic possibilities. *J Pathol* 247: 539–551

Roesch A, Fukunaga-Kalabis M, Schmidt EC, Zabierowski SE, Brafford PA, Vultur A, Basu D, Gimotty P, Vogt T, Herlyn M (2010) A temporarily distinct subpopulation of slow-cycling melanoma cells is required for continuous tumor growth. *Cell* 141: 583–594

Saftig P, Klumperman J (2009) Lysosome biogenesis and lysosomal membrane proteins: trafficking meets function. *Nat Rev Mol Cell Biol* 10: 623–635

Settembre C, Fraldi A, Medina DL, Ballabio A (2013) Signals from the lysosome: a control centre for cellular clearance and energy metabolism. *Nat Rev Mol Cell Biol* 14: 283–296

Shannon P, Markiel A, Ozier O, Baliga NS, Wang JT, Ramage D, Amin N, Schwikowski B, Ideker T (2003) Cytoscape: a software environment for integrated models of biomolecular interaction networks. *Genome Res* 13: 2498–2504

Sosman JA, Kim KB, Schuchter L, Gonzalez R, Pavlick AC, Weber JS, McArthur GA, Hutson TE, Moschos SJ, Flaherty KT *et al* (2012) Survival in BRAF V600-mutant advanced melanoma treated with vemurafenib. *N Engl J Med* 366: 707–714

Subramanian A, Tamayo P, Mootha VK, Mukherjee S, Ebert BL, Gillette MA, Paulovich A, Pomeroy SL, Golub TR, Lander ES *et al* (2005) Gene set enrichment analysis: a knowledge-based approach for interpreting genome-wide expression profiles. *Proc Natl Acad Sci USA* 102: 15545–15550

Tan JX, Finkel T (2022) A phosphoinositide signalling pathway mediates rapid lysosomal repair. *Nature* 609: 815–821

Tang Z, Kang B, Li C, Chen T, Zhang Z (2019) GEPIA2: an enhanced web server for large-scale expression profiling and interactive analysis. *Nucleic Acids Res* 47: W556–W560

Tanouchi A, Taniuchi K, Furihata M, Naganuma S, Dabanaka K, Kimura M, Watanabe R, Kohsaki T, Shimizu T, Saito M *et al* (2016) CCDC88A, a prognostic factor for human pancreatic cancers, promotes the motility and invasiveness of pancreatic cancer cells. *J Exp Clin Cancer Res* 35: 190

Tsukiyama T, Matsuda-Tsukiyama M, Bohgaki M, Terai S, Tanaka S, Hatakeyama S (2012) Ymer acts as a multifunctional regulator in nuclear factor-kappaB and Fas signaling pathways. *Mol Med* 18: 587–597

Villanueva J, Herlyn M (2008) Melanoma and the tumor microenvironment. *Curr Oncol Rep* 10: 439–446

Wang H, Zhang CZ, Lu SX, Zhang MF, Liu LL, Luo RZ, Yang X, Wang CH, Chen SL, He YF *et al* (2019) A coiled-coil domain containing 50 splice variant is modulated by serine/arginine-rich splicing factor 3 and promotes hepatocellular carcinoma in mice by the Ras signaling pathway. *Hepatology* 69: 179–195

Wang X, Wei Z, Lan T, He Y, Cheng B, Li R, Chen H, Li F, Liu G, Jiang B *et al* (2021) CCDC88A/GIV promotes HBV replication and progeny secretion via enhancing endosomal trafficking and blocking autophagic degradation. *Autophagy* 18: 357–374

Wei L, Jin Z, Yang S, Xu Y, Zhu Y, Ji Y (2018) TCGA-assembler 2: software pipeline for retrieval and processing of TCGA/CPTAC data. *Bioinformatics* 34: 1615–1617

Yang ZJ, Chee CE, Huang S, Sinicrope FA (2011) The role of autophagy in cancer: therapeutic implications. *Mol Cancer Ther* 10: 1533–1541

Yang L, Liu Q, Zhang X, Liu X, Zhou B, Chen J, Huang D, Li J, Li H, Chen F *et al* (2020) DNA of neutrophil extracellular traps promotes cancer metastasis via CCDC25. *Nature* 583: 133–138

Yin C, Zhu B, Zhang T, Liu T, Chen S, Liu Y, Li X, Miao X, Li S, Mi X *et al* (2019) Pharmacological targeting of STK19 inhibits oncogenic NRAS-driven melanomagenesis. *Cell* 176: 1113–1127.e16

Zeng WJ, Lu C, Shi Y, Wu C, Chen X, Li C, Yao J (2020) Initiation of stress granule assembly by rapid clustering of IGF2BP proteins upon osmotic shock. *Biochim Biophys Acta Mol Cell Res* 1867: 118795

Zhu Y, Qiu P, Ji Y (2014) TCGA-assembler: open-source software for retrieving and processing TCGA data. *Nat Methods* 11: 599–600

Zhu SY, Yao RQ, Li YX, Zhao PY, Ren C, Du XH, Yao YM (2020) Lysosomal quality control of cell fate: a novel therapeutic target for human diseases. *Cell Death Dis* 11: 817